Galaxy Morphology In Cluster Environments

by

Harisah Mehmood

A thesis
presented to the University of Waterloo
in fulfilment of the
thesis requirement for the degree of
Masters of Science
in
Physics

Waterloo, Ontario, Canada, 2017

Author's Declaration

This thesis consists of material all of which I authored or co-authored: see Statement of Contributions included in the thesis. This is a true copy of the thesis, including any required final revisions, as accepted by my examiners.

I understand that my thesis may be made electronically available to the public.

Statement of contributions

The modelling work in this thesis uses orbital libraries based on N-body simulations created by Kyle A. Oman. The entire modelling and analysis is my own work.

Abstract

It is a well known fact that cluster environments favour early-type galaxies over late-type. However, the physical origin of the correlation remains uncertain. We focus specifically on the external environmental mechanisms responsible for morphological transformation of late-type into early-type galaxies using $\sim$ 30,000 satellites in 625 clusters from SDSS DR7. All the external processes have one factor in common which is the orbital path taken by a satellite through the cluster that determines the extent of the environmental effects. We use results from orbital libraries extracted from N-body simulations. These give a probabilistic mapping between normalized projected phase-space (R, V) coordinates to lookback time to cluster infall. The look back time is the key ingredient that traces how far the satellite is in its orbit compared to the cluster centre. Using these results, we explore the effects of a decrease in disc luminosity caused by disc quenching and disc scale length reduction on satellite morphology quantified by the luminous bulge-to-total (B/T) ratio. Our findings suggest that satellites are quenched and their disc scale lengths are reduced after spending $\sim$ 5 Gyrs in the cluster which corresponds to $\sim$ 1 Gyr after passing the pericenter. A drop in disc luminosity due to these processes has a small impact on morphology suggesting that other active processes such as harassment are responsible for further morphological transformations. Fitting to account for such processes over and above the ones responsible for a drop in disc luminosity, we find that satellites with B/T < 0.1 (pure disc systems) experience most drastic changes: their structure changes by developing a bulge component $\sim$ 5 Gyrs after infall. Similarly, objects with $0.1 <$ B/T < 0.3, are affected by harassment over a longer time scale $\sim$ 7 Gyrs suggesting that satellites with a bulge component are more resistant to harassment compared to pure disc systems. We conclude that the density-morphology relationship is a manifestation of both hydrodynamical as well as gravitational processes driving late-type to early-type morphology.

Acknowledgements

I want to thank my supervisor, Dr. Michael Hudson, for his guidance throughout the work as well as my committee members Dr. Michael Balogh and Dr. Niayesh Afshordi for their useful suggestions and comments.

Dedication

For Mama, *Abo*, *Bari Ammi*, *Barey Abo* and *Khala*.

Table of Contents

List of Figures

List of Tables

List of Abbreviations

PPS: Projected phase-space

SPS: Stellar population synthesis

SFR: Star formation rate

SFH: Star formation history

SF-TT: Star formation truncation time

Chapter 1

Introduction

Galaxies are agglomerations of stars, dust, gas and dark matter, mostly harbouring a black hole in the centre, found throughout the universe. A closer look into them reveals a variety in their structure. This range of morphology was first classified by Hubble (1926) in the form of the Hubble tuning fork which divides galaxies into three morphological types: Elliptical, spirals (regular and barred) and lenticulars shown in Fig. 1.1. The left of this figure shows Ellipticals (denoted by E), lenticulars (denoted by S0) in the middle and spirals branching out into regular (denoted by S at the top) and barred-spirals (denoted by SB at the bottom) on the right. Ellipticals and lenticulars are usually referred to as early-type galaxies while spiral and irregulars are termed late-type.

As visible in Fig. 1.1 ellipticals galaxies tend to be featureless, smooth and red in color while spirals show a distinct spiral pattern, and are blue in color. The color of galaxies is primarily related to star formation activity. Spiral galaxies therefore have an active star formation history while ellipticals being red are considered 'dead' with regards to this.

This diversity in color and morphology leads to a natural curiosity behind the formation and evolution of such systems. One can ask two questions:

1. Do galaxies of different types have a common origin? If there is one, then how does one transform into the other?

2. If galaxies don't share a common origin then how does the present day diversity come into being?

Over the course of time, many observations have helped answer these questions. Bell et al. (2004) using COMBO-17 survey clarified that when plotted on a color-magnitude space, galaxies tend to cluster into two main groups: a red sequence and a blue cloud with a few objects sitting in the region between the two extremes, the

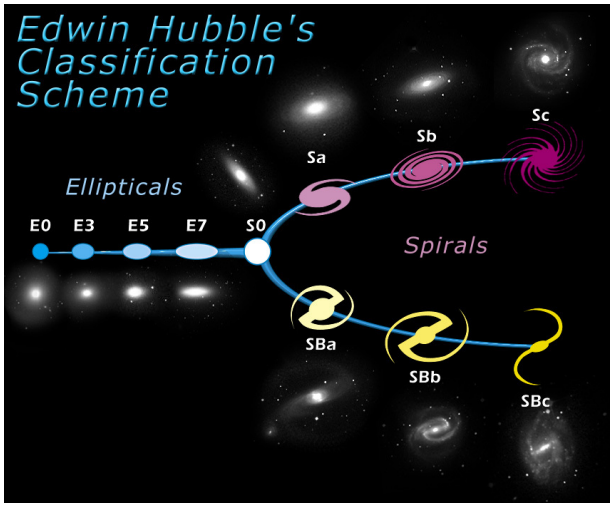

Figure 1.1: Hubble's morphological classification sequence showing galaxies evolving in complexity from left to right. This sequence is not meant to be read as an evolutionary sequence of ellipticals transforming into spirals via lenticulars. Courtesy *Wikipedia*.

green valley, as shown in Fig. 1.2. This bimodality was also previously observed in SDSS (Strateva et al., 2001) and in de Vaucouleur's (de Vaucouleurs, 1961) analysis of galaxy morphology. This suggests that fundamentally galaxies come in two types. Moreover, the Butcher-Oemler effect (Butcher and Oemler, 1978) shows the evolution in galaxies as a function of redshift. A large number of actively star forming and distorted/irregular blue galaxies are observed in the cores of clusters at z $\sim$ 0.4 which disappear in the present day clusters that favour a large population of elliptical galaxies. This signals an evolution in galaxies over time as well as that perhaps dense environments such as that of a cluster play a role in driving a dominant population of actively star forming spiral galaxies into dormant red ellipticals. These results taken together present a shared origin of galaxies where they can be fundamentally classified only into two groups suggesting that one transforms into the other.

In addition, a variety of other discoveries such as expansion of the universe (Perlmutter and Riess, 1999) and cosmic microwave background (CMB) (Penzias and Wilson, 1965) tipped the scales in favour of the Big Bang model of the universe suggesting that the universe had its beginnings set off by a gargantuan blast in extraordinarily hot conditions. The Lambda cold dark matter (ΛCDM) is the concordance model and is widely accepted due to its agreement with cosmic microwave background, large scale structure as well as accelerated expansion of the universe. This assumes a flat universe with $\sim$ 75 % energy due to cosmological constant, $\sim$ 21% due to 'cold' dark matter and remaining $\sim$ 4 % from baryonic matter. ΛCDM attempts to explain the structure formation as a result of quantum fluctuations.

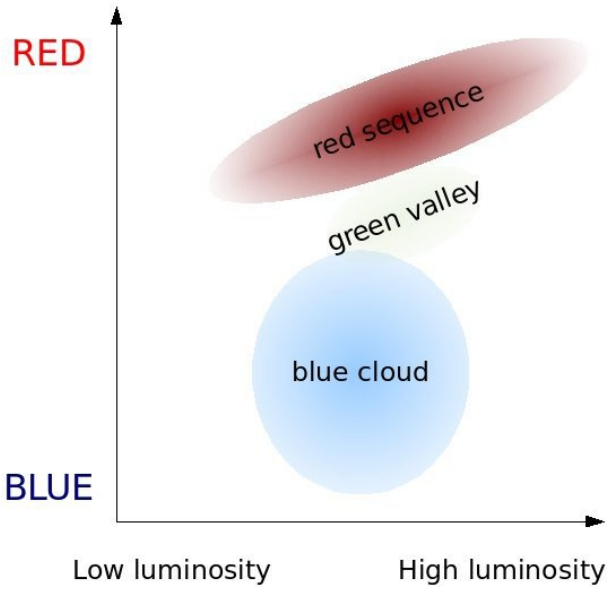

Figure 1.2: A schematic showing distribution of galaxies in color-magnitude space. This highlights galaxies mainly forming two fundamental types. Courtesy *Wikipedia*.

Due to the wide range success of this model, we work within the ΛCDM framework for the purpose of this thesis.

The goal of our study is to understand how galaxy morphology changes in the cluster environment as a function of the amount of time spent in the cluster. We use a combination of observational data and orbital libraries based on N-body simulations to achieve this. While internal mechanisms are important in galactic evolution, our focus is specifically on the external environmental mechanisms responsible for driving late-type spirals to early-type lenticulars in clusters.

We provide a brief overview of galaxy formation as widely accepted according to hierarchical structure formation in Sec. 1.1 as well as the internal mechanisms influencing galaxy evolution. We then look at how clusters seem to suggest transformation of one type of galaxy into another (Sec. 1.2). Galaxy evolution can be influenced by external mechanisms which we explore in Sec. 1.3. Our work specifically focuses on understanding how galaxy morphology evolves in a cluster influenced by external (environmental mechanisms). This requires a detailed view of satellite location which is possible via N-body simulations. We outline the connection between projected phase-space (from observations) and orbital history in Sec. 1.4 Finally, we lay down the objectives of this work in Sec. 1.5.

1.1 Galaxy Formation

In Big Bang model of the universe, the early universe was dominated by radiation where photons existed alongside protons and electrons in the form of photon-baryon fluid. At z $\sim$ 1100, as the universe cooled and electrons and protons combined into atoms, photons broke free from this fluid and propagated freely. This radiation, cosmic microwave background, as observed today has a temperature of about 2.7 K and is extremely uniform in all directions with variations on the order of $\sim 10^{-4}$. These variations are thought to be grown from quantum fluctuations and are understood to be the seeds from which the future structure in the universe developed. Different gravitational structures then condensed to form filaments and walls from which galaxy groups, clusters and superclusters are formed later.

Since dark matter particles interact only via gravity, once the universe expanded enough, the dark matter particles first formed inhomogeneities. This was possible due to gravitational Jean's instability where an overdense region can simply collapse under its own gravity and is not opposed by any other forces such as radiation pressure. As time progresses, the denser regions become denser and the rarefied ones become more 'empty'. In the early universe, the dark matter perturbations with different wavelengths all evolve independently. Since the universe was also expanding, the amplified fluctuations grow as a power law $\delta\rho/\rho \propto t^{\alpha}$ where $\alpha > 0$, instead of an exponential growth. Once the perturbations have attracted enough mass such that the density contrast with the background, $\delta\rho/\rho \sim 1$, the perturbation exits the linear regime and moves on to the non-linear regime. In the non-linear regime, the dark matter particles tend to cross each other's orbits and the processes of galaxy formation becomes more complicated with gas cooling and condensing inside the gravitational potential well of dark matter halos. Press and Schechter (1974) first calculated the mass function of galaxies within non-linear structure growth.

Many internal processes such as gas cooling, star formation, feedback processes and merger in the early history of galaxy formation all contribute to the structure of galaxies visible today. Gas cooling plays an important role as it depends on the temperature, density and variety of cooling processes. The cooled gas later segregates and accumulates onto the protogalaxy. It collapses under its self gravity and eventually form stars. The process of star formation does not always proceed in a straightforward way. There are many feedback processes that can impede this growth. Supernovae (SNe) produce enormous amounts of energy, thus reheating the cold gas. Similarly, a galaxy can also lose material including both gas and stellar mass via stellar winds caused by SNe (Dekel and Silk (1986); Damjanov et al. (2009)). Another significant source of feedback comes from active-galactic nuclei (AGN)(Croton et al., 2006; McNamara et al., 2006) that can also be responsible for reheating the gas preventing it from cooling. While it is known that all such

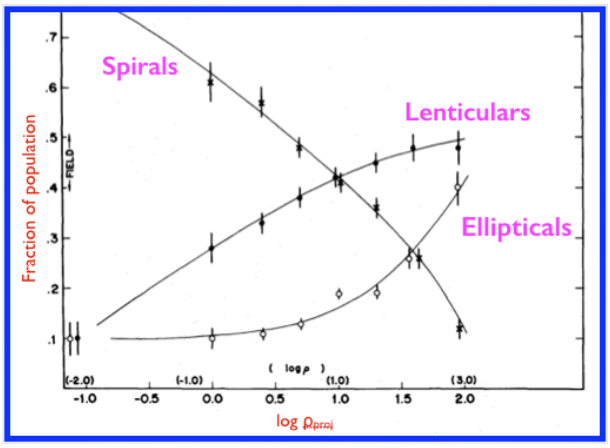

Figure 1.3: The figure shows fraction of population of spirals, irregulars and ellipticals as a function of projected density showing an increase in ellipticals and lenticulars while a drop in spirals toward cluster centre. Figure obtained from Dressler 1980.

processes play a significant role in galaxy formation, it is still not understood as to how much they dominate and when and how they all contribute toward galaxy formation.

Since galaxies are not completely isolated, not only do they affect their environment (in terms of outflows) but also get influenced by it. In the CDM cosmology, the dark matter halos grow hierarchically such that larger halos form from the coalescence of smaller progenitors via merging. The outcome of a merger thus also plays a significant role in galaxy formation. It is thus a very challenging processes to separate out the dominant process playing a role in galaxy evolution. But regardless, the environment also plays a role in determining the eventual fate of galaxies.

1.2 Galaxies And Their Environment

It has been known since 1935 that galaxies and their environment might be interconnected (Smith, 1935; Zwicky, 1942; Sandage, 1961). Denser environments favour elliptical and lenticular galaxies over spirals which are found in abundance in low density regions. Dressler (1980) showed that the fraction of ellipticals and lenticulars increases to $\sim$ 40 and 50% respectively compared to that of spirals which drops to 10 % (see Fig. 1.3) towards cluster centre. This density-morphology relationship has been at the forefront of understanding galaxy evolution studies (as mentioned earlier, guided by a line of observational evidence).

In addition to exhibiting a stronger evolutionary signature in morphology, galaxies in dense environments are redder due to decreased star formation activity (Balogh

et al., 2004; Hogg et al., 2004), and are less gas-rich with lower specific star formation. Satellites in groups/clusters have a higher red sequence fraction, in fact, as much as one third of the red-sequence build up can be attributed to satellite galaxies (van den Bosch et al., 2008; Tinker and Wetzel, 2010). Combined with the color of elliptical galaxies in dense environments, the two seem promising physical quantities to help guide our understanding of galaxy evolution in dense environments such as those provided by clusters.

Cluster environments are the largest gravitationally bound and one of the most virialized systems in the universe with masses ranging from $10^{13} - 10^{15} M_{\odot}$ and sizes between $\sim 0.5-2$ Mpc. A cluster can consist of anywhere between 20 to 1000 luminous galaxies, hot gas plasma that emits X-ray radiation with temperatures $10^7 - 10^8$K constituting the intracluster medium (ICM) and dark matter particles dispersed as a halo. Since they are the densest and populous regions as well, they are also perfect laboratories providing us a snapshot of its constituent galaxies at different stages in their evolutionary cycle. Satellites recently falling in are generally expected to lie at the periphery while those that have been in the cluster for a while would be expected to lie at the bottom of the potential well. This is due to dynamical friction which is responsible for the loss of angular momentum from a galaxy as part of its forward motion is transferred to the random motion of the stars of a galaxy passing by. This loss of momentum and kinetic energy means that once a galaxy passes through the pericentre and is on its way back to the apocentre, it would not reach all the way back to its original apocentre. Instead, it will now have a new apocentre closer to the pericentre due to the decreased orbital motion (Bertschinger, 1985). We will come back to this in Sec. 1.4

Since interactions with other galaxies are likely common in cluster, although not as common as group environments, these interactions are bound to influence galaxies. Thus, galaxy evolution can be attributed to both internal and external (environmental) processes and the interplay of both processes leads to the current observed state of satellites. In this project, the aim is to study the external environmental effects on galaxies within cluster environments.

1.3 Environmental Processes

Galaxies falling into the cluster environment are subject to the hot plasma gas and the tugs of neighbouring galaxies. Some important processes due to the overall effect of the cluster and its members on satellite galaxies are listed below. Most of the material below is adapted from Mo et al. (2010).

1.3.1 Ram Pressure Stripping (RPS)

Ram pressure stripping (Gunn and Gott, 1972) occurs as an infalling galaxy makes its way through the hot cluster plasma where the pressure exerted by the intracluster medium (ICM) on its interstellar medium (ISM) is felt as a wind (Gunn and Gott, 1972; Abadi et al., 1999; Chung et al., 2007; Jáchym et al., 2007; Smith et al., 2010b). This effect drives gas out of the galaxy, forming a tail in the opposite direction to the galaxy's motion. If the density of ICM is given by ρ_{ICM} and the velocity of the galaxy moving through the cluster as V then the pressure exerted by the ICM is simply, $P_{ram} = \rho_{ICM} V^2$. If this pressure exceeds the force per unit area of binding the ISM to the galactic disc then the galaxy will end up losing its gas to the ICM as long as the following condition is met:

$$\rho_{ICM} > \frac{2\pi G \Sigma_* \Sigma_{ISM}}{V^2} \tag{1.1}$$

where Σ_{ISM} is the surface density of interstellar gas and Σ_* is the mean mass density of the disk. This gas deprivation will result in star formation quenching over time and, for this reason, ram pressure stripping is usually considered a likely mechanism responsible for a decline in star formation for cluster satellites. Since the ram pressure is based on the density of ICM, which changes as a function of cluster-centric distance (being the highest near the cluster centre), as well the velocity of the satellites, which also changes as satellite traverses through the cluster, the ram pressure also changes. Thus, a given satellite experiences different amount of stripping based on its location within the cluster. In addition to location, the eccentricity of the satellite's orbit as well as the inclination angle of the satellite disc and its orbital plane also plays a vital role in determining the effect of ram pressure stripping. A satellite that falls face-on into cluster will experience more stripping.

An RPS event can also lead to a star burst event due to the compression of the ISM (Owen et al., 2006; Cortese et al., 2007; Owers et al., 2012; Ebeling et al., 2014). Similarly, the stripped gas can also form stars in the wake of the galaxy, loosely termed as 'fireball' (Yoshida et al., 2008; Kenney et al., 2014).

1.3.2 Strangulation

RPS mainly removes the cold disc gas from the galaxy leading to a sudden cessation of star formation activity. The outermost hot gas envelope of galaxy is in fact more susceptible to tidal or ram pressure stripping as it is loosely bound. If the outer hot gas halo is removed, the future fuel reservoir of star formation is stripped off and this process is called strangulation (Larson et al., 1980; Balogh et al., 2000; McCarthy et al., 2008; Font et al., 2008). Strangulation would affect the star formation activity

at a later time than ram pressure stripping. This is due to the fact that if hot halo gas is removed via strangulation then cold disc gas is still forming stars.

1.3.3 Harassment

Satellites in a cluster usually have velocities $\sim 1000 - 1500$ km/s which is much greater than their internal velocity dispersion. Thus, high speed tidal encounters occur frequently with neighbouring galaxies. The cumulative effect of these in addition to the cluster potential is called harassment (Farouki and Shapiro, 1981; Moore et al., 1996; Smith et al., 2010a). The strong close encounters lead to a loss of angular momentum via transference to the galaxy's own dark matter halo and the perturbing galaxies. In the event of a strong encounter where mass could be tidally stripped, the result is that the satellite becomes less bound, leading to the formation of a prolate flattened shape where the motion of stars are now rearranged into a random fashion. Thus, harassment could manifest itself as a galaxy being puffed up. While the rearrangement changes the overall shape of the galaxy, it can also funnel either gas mass or stellar mass or a combination of both into the central regions of the galaxy from the disc. In case of gas mass being transferred, star burst could ensue due to the enhanced pressure as gas sinks into the deeper potential well. On the contrary, if the satellite is devoid of gas, stellar mass could also be rearranged such that if a satellite had a large disc component at infall, then, due to harassment, stellar mass from the disc would be pushed toward the central regions causing the formation of a stellar bulge.

Harassment is a non-collisional processes where the impact of harassment depends on the square of the masses of the largest galaxies encountered. In extreme cases, as found by Moore et al. (1998), late-type (Sc-Sd) spiral galaxies could encounter enough impulsive heating due to harassment that some stars are pushed into unbound orbits. Moore et al. (1996, 1998) further showed that satellites on eccentric orbits exhibit stronger change to their overall mass after first pericentric passage compared to those on circular orbits.

1.3.4 Tidal Stripping

Other gravitational processes include tidal stripping (Mayer et al., 2006) which is the removal of mass starting from the outermost dark matter halo. In some cases if the pull is strong enough then the disc gas, and in extreme cases entire stars, can be pulled out of their orbit from a satellite. Tidal stripping is dependent on the tidal radius of a satellite orbiting within an larger subhalo which is defined as:

$$r_t = \left[\frac{m/M}{(3+m/M)}\right]^{1/3} R \tag{1.2}$$

where r_t is the tidal radius, m the mass of satellite orbiting around the potential well of a larger subhalo, M. If the tidal acceleration, $2GMr/R^3$ (where R is the orbital radius of m around M), by M exceeds the binding force per unit mass of m, Gm/r^2, then the material past r_t will be stripped away. The tidally stripped material in some cases is seen as tidal tails.

1.3.5 Mergers and Cannabalism

Galaxy mergers (Toomre and Toomre, 1972; Cox et al., 2006) are events whereby two or more galaxies collide leading to the formation of new structure. Such an event is possible if the orbital energy of the interacting objects is low where an interaction could lead to a merger. The collision mainly involves gravitational attraction between the galaxies and friction between the gas and dust particles that is largely responsible for the final shape of the newly formed system. In a merger, the orbital energy of the interacting galaxies is transferred into the internal energy which can be transferred to the dark matter halo or carried away in an event of tidal mass loss.

Due to the high encounter speed of satellites within clusters, merger events tend to be rare, but are more common in groups. For a cluster environment, these become important in situations where infalling galaxies fall together in groups and due to the interactions amongst themselves could possibly undergo a merger event while still near the cluster periphery.

Similarly, galactic cannibalism is a processes whereby satellites that have lost energy and momentum due to dynamical friction, sink towards the centre of the cluster potential well and merge with the central cluster galaxy possibly leading to the formation of a cD galaxy (Ostriker and Tremaine, 1975; Hausman and Ostriker, 1978). Since this process involves destruction of galaxies, presumably equally of all types (visible in the outer diffused envelope), cannibalism cannot be responsible for the increase in the quenched population.

1.4 Linking Orbital Path To Phase-Space Coordinates

Previous studies have studied the effects of cluster environment as a function of cluster-centric distance. Similarly, the environment of galaxies has also been quantified as N^{th} nearest neighbour of a galaxy. While these measures of environment

serve the purpose well, they do not however disentangle different satellites due to projection effects. To explain this further, as mentioned earlier, a satellite loses its orbital energy as it traverses through the cluster environment. If, for example, one wants to separate out the recent infalling objects in the cluster, a simple cut based on the farthest distance from the cluster centre would allow for this. But this spatial region will also include satellites that have completed their first pass through the pericentre and are just reaching apocentre. Thus, a simple spatial division is not ideal.

To understand the origin and evolution of color and morphology of cluster satellites, it becomes important to understand which processes occur when and eventually how they all add up to produce the current state of satellites. Interestingly, all the environmental processes mentioned previously are sensitive to the path taken by the satellite through the cluster. Information on satellite path becomes important since different processes are more effective at different locations within the cluster such as ram pressure stripping and harassment which are both expected to be the strongest near the cluster core i.e., the pericentre. Observationally, however, we are limited to measuring three of the six phase-space coordinates, a projected radius, R_{proj}, and a line-of-sight velocity, V_{los}, missing direct insight into the orbital history. A view into the orbital history is however possible by linking distinct regions of phase-space with different amounts of time spent in a cluster which was first introduced by Gill et al. (2005). This was simulated by Mahajan et al. (2011) and Oman et al. (2013), hereafter O13. Thus, while projected phase-space hides the orbital history, it provides enough information to be linked with the amount of time spent in a cluster which becomes an extremely useful tool in helping identify the dominant processes at work. In this work, we use orbital libraries created by O13 that provide us a probabilistic mapping between projected phase-space coordinates and lookback to infall time. This will be discussed in detail in Chap. 2.

1.5 Objective

For the purpose of this thesis, we study how the morphology of satellites changes as a function of time since infall. While Hubble classification allows for a subjective assigning of galaxies, a bulge-to-total ratio is a more quantitative form of morphology classification which we adopt here given as B/T = bulge/bulge+disk. We focus specifically on the environmental mechanisms that could affect morphology, driving star-forming disc-dominant galaxies into quiescent bulge-dominant systems. Several authors have shown that satellites experience quenching due to gas loss or consumption. Moreover, Hudson et al. (2010) showed that disc colours of satellites become increasingly red as a function of cluster-centric distance whereas the bulge colours remain uniformly red throughout. Thus, discs are strongly quenched by clusters. Quenching could have an impact on morphology in that a faded disc (a drop in disc

luminosity) would lead to an apparent increase in B/T. Similarly, reduction in disc luminosity can also be an outcome of a physical signature such as reduction in disc scale length e.g., due to tidal mass loss. In our model, we therefore first consider how the discs are affected by processes involving a decrease in disc luminosity as a function of infall time and then attempt to understand the impact of these on the morphology by generating a predicted B/T distribution. We then model the excess morphological changes over and above not accounted for via a drop in disc luminosity.

We discuss our data set in Chap. 2. A brief outline of the model is provided after which leads into explaining the three different steps of the model explained in Chap. 3−5. Finally, we summarize, conclude and mention future directions in Chap. 6

Chapter 2

Data

To obtain a large sample of cluster satellites with interlopers, we use data from Sloan Digital Sky Survey, DR7 (Abazajian et al. (2009)) with apparent magnitude limit: $m_r \geq 17.77$ and cluster catalogue provided by von der Linden et al. (2007). This catalogue consists of 625 clusters with a total of 49,107 satellites within a projected radius (measured with respect to the cluster centre), $R_{proj} < 2.5r_{vir}$, and measured line-of-sight velocity, $V_{los} < 2.0\sigma_{3D}$, where r_{vir} is the 3D virial radius [1] and σ_{3D} is the 3D velocity dispersion of the cluster, see O13 for details. We use normalized coordinates defined as: projected radius, $R = R_{proj}/r_{vir}$ and line-of-sight velocity: $V = V_{los}/\sigma_{3D}$ to be used throughout the rest of the work. The data is furthermore supplemented with bulge-disc decomposition of satellites obtained from the catalogue by Simard et al. (2011) while stellar mass bulge-disc decompositions are taken from Mendel et al. (2014).

2.1 Cluster Satellite Sample

We remove brightest cluster galaxies, BCGs, as there is no counterpart for them in the orbital libraries (see Sec. 2.3). Galaxies with missing data for all of: bulge-to-total (B/T), bulge magnitude, disc magnitude and disc scale length are also removed. If a galaxy is only missing one of these quantities, it is kept in our sample. This cleaning reduces the number of satellites down to 48,454. To determine a BCG in a given cluster, we find satellites with the smallest R in a given cluster since von der Linden et al. (2007) specify the location of the BCGs as R=0. We find that all 625 clusters have a member within: $0.0 \leq R \leq 0.35$. To ensure we only remove objects with $R \sim 0$, we remove 454 galaxies with: $0.0 \leq R \leq 0.00875$.

[1] The virial radius is defined as the radius enclosing a region with an overdensity of 360 times the background density at z=0

Below we describe the data set in detail.

2.2 Morphological Data

Morphological data are from Simard et al. (2011), who perform two-dimensional bulge-disc photometric decompositions for over one million objects from Legacy area of the SDSS-DR7 survey using Galaxy Image 2D (Simard, 1998, GIM2D). They perform simultaneous fits in g and r-bandpasses by enforcing the bulge radius, ellipticity and position angle, and the disk scale length, inclination and position angle to be the same in both bands. This method reduces the error in the fits but also makes them insensitive to colour gradients. Their decomposition method is based on fitting three different models: a pure Sérsic model, a de Vaucouleurs bulge (Sérsic index $n_b = 4$) + a pure exponential disk (hereafter $n4$ model), and a Sérsic (free-n_b where n_b is the bulge Sérsic index) bulge + exponential disc model (hereafter free-n_b model). However, they point out that the bulge-disc decompositions are more reliable for the $n4$ model. We also find the $n4$ fits to be consistent with visual inspection in the sense that for satellites that are fit with a large bulge component in the free-n_b model were visually found to have a small bulge component accounted for by the $n4$ fits. Thus, we choose the $n4$ model for the rest of the analysis (see Appendix A). Their catalogue provides a variety of physical quantities including, g and r-band magnitudes for bulge, disc and entire galaxy, disc scale length, inclination angle, luminous B/T etc. that we make use of in this paper. We also reassign the B/T such that all satellites with B/T< 0.1 were changed to B/T $= 0$ and those with B/T > 0.9 were assigned a B/T$= 1$ because the colors of small components were found to be unreliable (see Appendix B).

To obtain bulge-disc decompositions in stellar mass we use the catalogue provided by Mendel et al. (2014). This catalogue is based on the g and r-band photometric fits by Simard et al. (2011) which they extended with the addition of u, i and z bands in order to perform multi-wavelength photometry to fit the broadband spectral energy distributions (SEDs) using stellar population synthesis (SPS) models. The uncertainty quoted in the total, bulge and disc stellar mass from their catalogue is ~ 0.15 dex. We use the stellar masses that account for internal attenuation from dust. Note that the Mendel et al. (2014) catalogue is incomplete due the fact that the profiles failed to converge in some cases while the fits were contaminated by a nearby object in others. Therefore when we match it to the satellites in our sample, we are left with 47,757 satellites.

Furthermore, we limit our number of satellites because O13 orbital libraries require a dark matter subhalo mass limit of $10^{11.9}$ $M_\odot$ to ensure a sample complete in satellite mass that is least sensitive to artificial disruption (Klypin et al., 1999; Kitzbichler and White, 2008). This also restricts usage of the libraries to only those

Selection Criterion	Number of satellites
BCGs and nonsensical value removal	48,454
Mendel catalogue cross-correlation	47,757
Mass cut to match with orbital libraries	30,682

Table 2.1: Table showing several criterion responsible for a reduction in the number of satellites in our sample. von der Linden et al. (2007) catalogue matched with O13 gives us a total of 49,107 objects to begin with.

satellites with DM masses of $\sim 10^{11.9} M_{\odot}$ or greater, which translates to $10^{10.3} M_{\odot}$ in stellar mass (Hudson et al., 2015). When we apply this cut to the data, we obtain a final sample size of 30,682 satellites. See Tab. 2.1 for a summary of the selection criterion applied to our data set.

2.3 Modelling using N-body Orbit Libraries

In order to get infall time for satellites in our sample, we use orbital libraries provided by O13. The libraries are constructed from the output of the MultiDark Run 1 (Prada et al., 2012, MDR1) dark matter-only cosmological N-body simulation. O13 compile a catalogue of the orbits of satellite haloes that tracks the haloes up to a distance of 2.5 r_{vir}. The choice of tracking the orbits upto $2.5r_{vir}$ allows inclusion of backsplash satellites [2].

The orbital libraries serve as a bridge between the observed projected phase-space coordinates and the look back time to infall into the cluster, which is defined at a crossing of $2.5r_{vir}$. For the purpose of our work, the orbital libraries take in (R, V), and provide a probability that a given satellite has a lookback to infall time. The lookback time is the key ingredient that traces the location of the satellite in its orbit relative to the cluster centre. O13 provides an estimate for the satellites in the libraries and gives a time of ~ 3 Gyrs after infall for satellites to reach r_{vir} and ~ 4 Gyrs after infall to reach the pericentre. Thus, having an estimate of the infall time (and therefore the location of the satellite) helps in determining the environmental processes that could be responsible for changing morphology.

For a realistic interpretation of the satellite properties in clusters today, it is important to understand that these satellites could have lived in smaller dense regions such as groups before their infall into the present day (z=0) host. Hence, the effect of the previous host affects the galaxy, called 'pre-processing'. The orbital libraries we use track the orbital history with respect to the final (z=0) host i.e., they ignore "group pre-processing" and isolate the effect of the present day host. But our model

[2] satellites that have crossed r_{vir} after completing their first pass through the pericentre on their way back to apocentre

accounts for the pre-processed fraction as will be elaborated later in Chapters 3− 5.

The simulations are based on Wilkinson Microwave Anisotropy Probe WMAP7 with $\Omega_m = 0.27$, $\Omega_\lambda = 0.73$, $\Omega_b = 0.73$, $n_S = 0.95$, h_o=0.70, $\sigma_8 = 0.82$. See O13 and Oman and Hudson (2016) for more details.

2.4 Projected phase-space (PPS)

Since our objective is to understand how the morphology of a satellite changes after infall into cluster as a function of the amount of time spent in it, we separate out different satellite populations based on their projected phase-space coordinates in the cluster. To do so, we bin satellites based on (R, V). Later we will model the effects of the cluster environment on a population of 'infalling' galaxies used as a control or reference sample. These infalling galaxies will be drawn from the population at large R and large V. Our model will assume that a change in galaxy properties occurs after some delay time and therefore will affect galaxies at different location in PPS differently. We split up the data set into nine projected phase-space bins (PPS bins from here onwards). The PPS binning is motivated by the results of O13 who demonstrate that if a particular population of satellites is of interest, it is possible to choose a region of phase-space that maximizes the likelihood of correctly assigning infall time into the cluster, t_{infall}.

Since our approach involves studying populations in PPS bins, it is useful to understand the probability that the galaxies have a given infall time. Fig. 2.1 shows the infall time probability density function for all PPS bins, also printed on each PPS bin is the interloper probability, $P_{\rm INT}$. These interlopers are defined as objects with $R < 2.5$ and $V < 2.0$ but $r > 2.5r_{vir}$ i.e., objects that have not fallen into the cluster yet and will either fall into it at a later time or will move onto another cluster. The orbital libraries include ~ 50 % interlopers.

To provide further intuition re the PPS and infall time, we also show the fraction of satellites in our sample with an infall time greater than ~ 5 Gyrs (top) and 7 Gyrs (bottom) and their projected phase-space location in Fig. 2.2. The white vertical and horizontal lines shows the PPS binning that we adopt throughout the thesis (*Extended PPS*, see Sec. 2.5). Although this PPS binning choice is conceptually and visually intuitive, it can be seen in the oldest, virialized population (bottom left PPS bin) that this bin contains a range of infall times. This shows that population disentanglement in PPS is improved if the PPS is binned diagonally as it can be seen in the blue colour on both panels. For this reason, we consider the *Diagonal* PPS binning to be the optimum choice. We elaborate on different PPS binning scheme and the choice of infalling and virialized PPS bins in Sec. 2.5. We again stress here that for graphical purposes we will use *Extended* PPS binning but we report results from the *Diagonal* PPS binning unless otherwise stated.

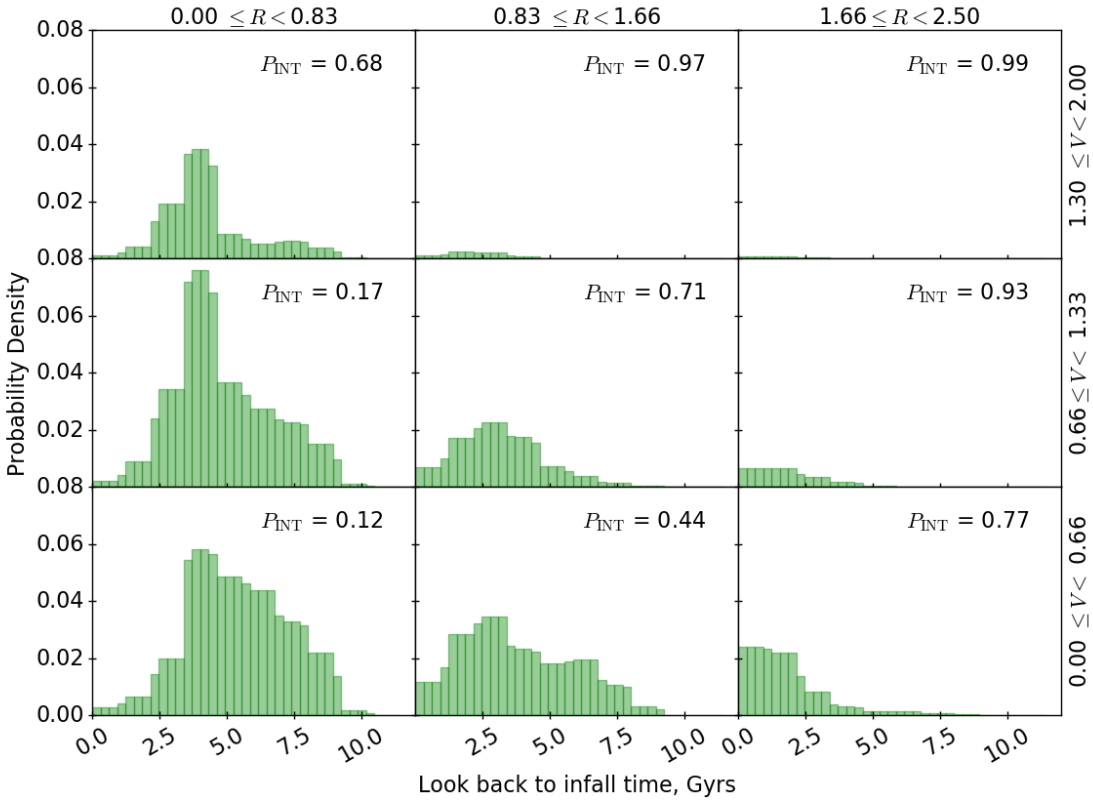

Figure 2.1: Average probability density for galaxies in a given PPS bin. Each panel represents a different bin in PPS with R increasing to the right and V increasing from bottom up. The interloper probability is printed as $P_{\rm INT}$ on each bin. As can be seen, the interloper probability is highest for the second and third bin in the first row as well as the third bin in the second row making the infalling population we use in our model (see Sec. 1.3).

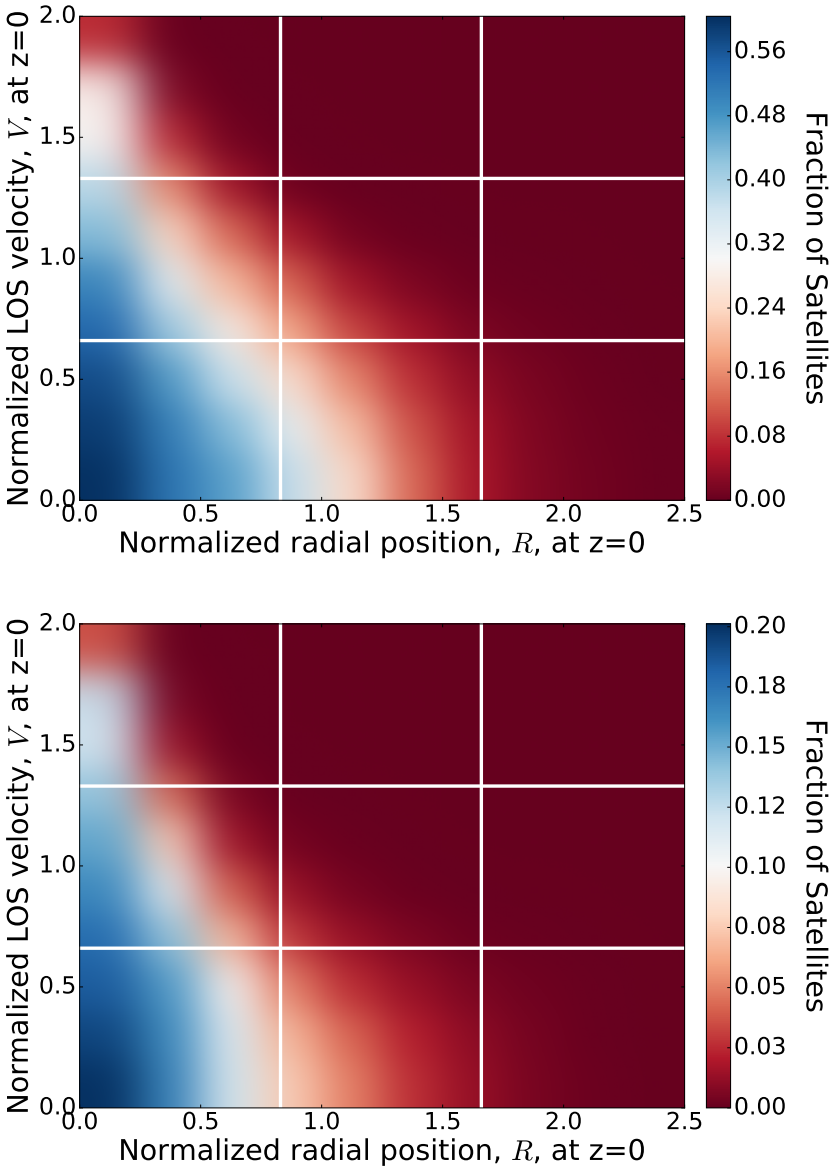

Figure 2.2: Fraction of satellites in the entire PPS of our sample ($0 \leq R \leq 2.5$ and $0 \leq V \leq 2.0$) with an infall time greater than $\sim$ 5 Gyrs (top) and infall time greater than $\sim$ 7 Gyrs (bottom). This shows the projected location occupied by satellites that are quenched (top) and the ones that are transformed into the early-type population i.e., have a B/T >0.3 (see Sec. 5.4). The white horizontal and vertical lines correspond to the *Extended* PPS binning (see Sec. 2.5).

To see how the goal of our study about understanding the evolution of morphology is related to the PPS bins, in Fig. 2.3, we show the r-band B/T distribution for different PPS bins from the *Extended* PPS-binning scheme (see Sec. 2.5). The red histogram represents the distribution from the entire sample (without any PPS cuts, hereafter global sample) whereas the blue data points are the bin-specific values. Vertical hatched lines are drawn at the median of the distributions and the error in the median is calculated from 1000 bootstrapped samples. We perform a Kolmogrov-Smirnov (KS) test between the global sample and the bin specific sample to check whether the PPS splitting is statistically significant. The p-value from this test is 0.00 for PPS bins of interest namely, the one on the top right (dominated by late type galaxies, hereafter the infalling population consisting mostly of satellites that have yet to fall into the cluster, the interlopers) and the other one on the bottom left (dominated by early type galaxies, hereafter the virialized population). Hence we reject the null hypothesis that global and bin specific populations are the same. This shows that populations in different PPS bins exhibit different morphologies.

In order to work with better statistics, we include the middle PPS bin in the top row and the rightmost PPS bin from the second row of Fig. 2.3 in our definition of infalling population, in addition to the PPS bin on the top left corner. This choice of infalling population is motivated by the fact that all three bins include more than 90 % interloper population (see Fig. 2.1, with interloper population printed on each PPS bin).

2.5 Different PPS-binning Schemes

In order to see if our results are sensitive to the way the data binning is done, we adopt four different PPS-binning schemes.

1- *Extended PPS*: All the plots shown in this paper follow this PPS binning unless otherwise stated. This includes the entire data set from the projected phase-space (R<2.5 and V<2.0) split into nine PPS bins (see top panel in Fig. 2.4).

2- *Restricted PPS*: We restrict the spatial cut to R <2.4 and velocity to V <1.2 and redivide the phase-space ranges into three equal bins. This was done since there are extremely fewer objects with $V > 1.2$ (see Fig. 2.4). This has the disadvantage that the total number of objects in the virialized population in this case drops to 4361 compared to the *Extended-PPS* case where there are 6464 objects. But has the advantage that all 9 PPS bins contain fairly large number of satellites. For this case, the definitions of infalling and virialized populations is the same as *Extended PPS* binning.

3- *Diagonal PPS*: This phase space binning was motivated by O13 where they showed that satellites belonging to different infall populations have diagonal pat-

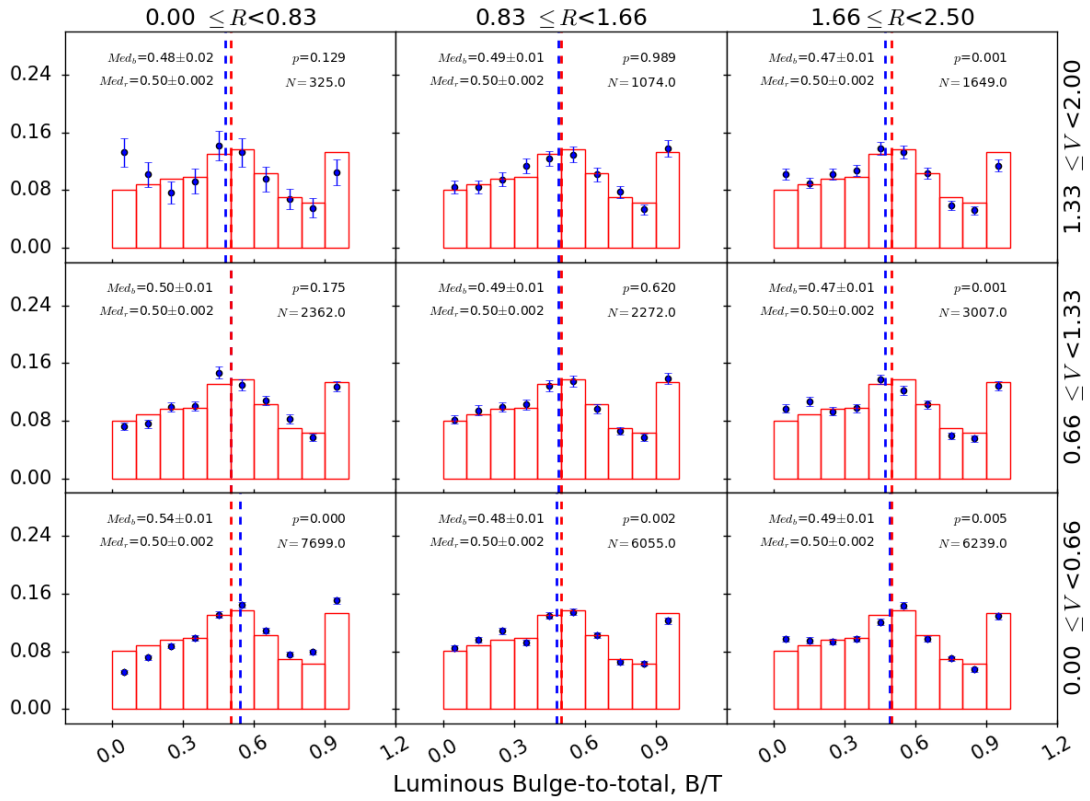

Figure 2.3: Bulge-to-total (B/T) distribution of galaxies from Simard et al. 2011 using their $n4$ model for *Extended* PPS binning. The red histogram shows data from all nine PPS bins (the global sample) and the blue data points show bin-specific values. Vertical hatched lines are drawn at the medians of the two distributions and each bin is labelled with the number of objects, N, the p-value from the Kolmogorov-Smirnov (KS) test, median values for the global (Med_r) and bin specific (Med_b) distributions along with their uncertainties obtained by 1000 bootstrap samples (see Sec. 2.2).

terns in projected phase-space (see their fig. 4; also discussed in 2.4, see Fig. 2.2). Similarly, O13, fig. 4.5 showed that probability past pericenter increases in a diagonal fashion. Older objects tend to sit below the diagonal with virialized population in the bottom left corner. We use their slope (-4/3) for the diagonal setup and split the entire phase-space into diagonal sections such that the diagonal width remains the same. See Fig. 2.4 (middle panel) that shows our entire data set split into diagonal bins. In this case, we took the infalling population to be consisting of the last two bins on top right while the virialized population is the bin on the bottom left.

The results from this binning should be superior to any other PPS binning choice for the reason that this allows for the cleanest separation of the infalling population but for reasons of difficulty of presenting results in a clear phase-space diagram, we don't show results but include them in all our tables.

4- *Equal Number PPS*: This binning involves splitting up the phase-space such that there are roughly equal number of objects in each one of the PPS bins. Fig. 2.4 (bottom panel) shows the the dimensions of each PPS bin as well as the number of objects in it. Again, the infalling and virialized populations are the same as *Extended PPS* binning.

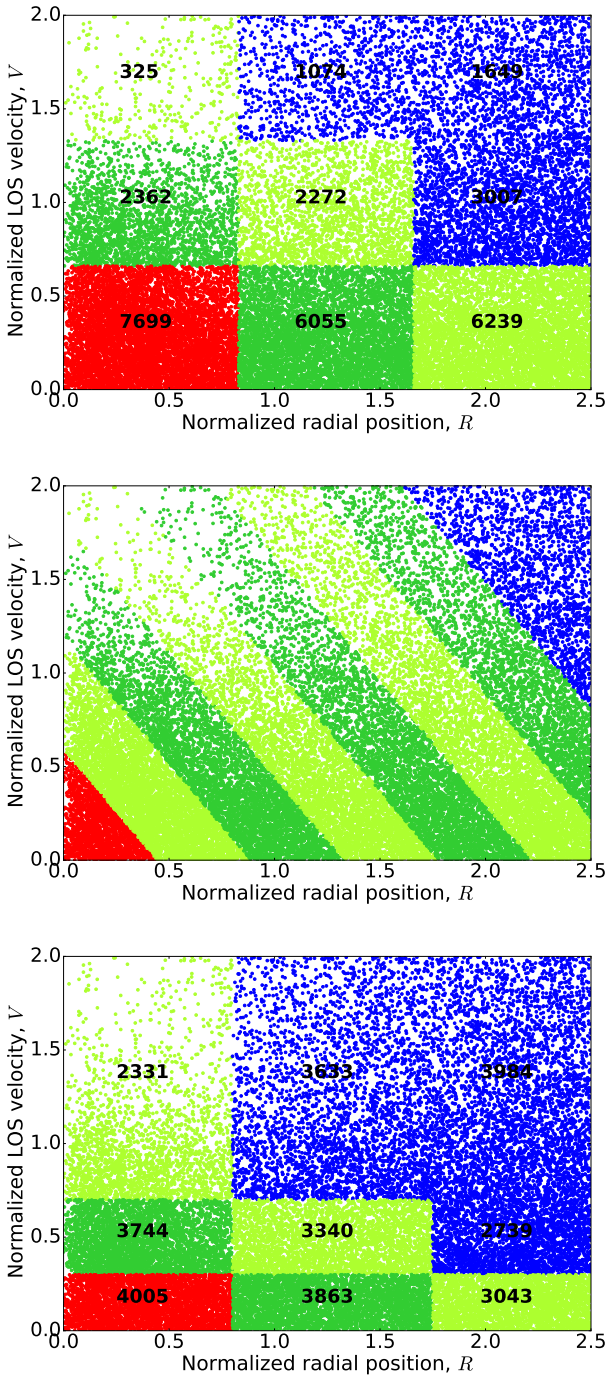

Figure 2.4: *Extended* PPS binning used throughout the thesis mainly for graphical purposes is shown on the top while *Diagonal* PPS (middle) and *Equal Number* PPS (bottom) binning are also shown. In each case, the infalling population is coloured blue and the virialized is coloured red. *Restricted* PPS binning is not shown since it is similar to *Extended* in that the entire phase-space is split into equal sized bins in R and V. The number of objects in each PPS bin for *Extended* and *Equal* is also printed in black.

Model Overview

Satellites in the cluster environment are subject to a variety of external mechanisms that are responsible for affecting them such as ram pressure stripping, strangulation, tidal stripping and harassment, to name a few. We model the effects of these processes by considering a delay time during which satellites remain unaffected by one or more of the processes (or a combination of them) and after which they are influenced by the cluster.

Several authors (Hogg et al. 2004, Balogh et al. 2004) have shown that satellites are more 'red and dead' than their field counterparts. More specifically, Hudson et al. (2010) found that disc colours of satellites become increasingly red as a function of cluster-centric distance whereas the bulge colours remain uniformly red throughout consistent with a model in which discs are strongly quenched. Since a galactic disc's luminosity, $L = 2\pi I_0 R_d^2$, is affected both by the central surface brightness, I_0, and disc scale length, R_d, any change in any of these quantities would have a direct impact on the disc luminosity. Quenching in this case would impact I_0 while a reduction in disc scale length e.g., caused by 'arrested-development' where the disc growth inhibited since infall into cluster would effect R_d. A decrease in disc luminosity would have a direct impact on morphology in that it would lead to an increase in B/T. To account for such changes, we build a model where we first consider how the discs are affected by processes involving a drop in disc luminosity as a function of infall time and then attempt to understand the impact of these on galaxy morphology by generating a predicted B/T distribution. We then account for excess morphological changes over and above those caused by a drop in disc luminosity in the third part of the model. We briefly outline the three steps of our model below.

1. First we model disc quenching by the cluster at a time, Δt_Q, the delay time between the infall into cluster ($r < 2.5 r_{vir}$) and the onset of quenching. Since colour indicates quenching, we fit for Δt_Q by matching the predicted disc colour distribution of satellites to that from observations in all PPS bins (see Chap. 3).

2. Second, we independently match the disc scale lengths from prediction to

observation by fitting for a timescale, Δt_{ST}, the delay time between infall into the cluster and the onset of disc scale length reduction (see Chap. 4).

3. The third part of the model involves finding the time, Δt_{MT}, at which the late-type satellites processed by quenching and disc size reduction are transformed into early-type. This is done in two steps. First we generate a model B/T distribution after calculating the effects of quenching and disc scale length reduction at their respective times and then a fraction of early-type satellites from the B/T distribution is passed into the second phase of the model that determines when the processed late-type satellites are transformed into early-type (the exact definition of late-type and early-type will be elaborated later, see Chap. 5).

In the following three chapters, we expand on each one of the modelling steps in detail. Each step is given a chapter of its own including results and discussion.

Chapter 3

Disc Quenching

We model disc quenching to the satellites such that the entire disc is faded altogether at the same time and by the same amount after spending a time, Δt_Q, the delay time between infall into the cluster (marked by the crossing of $2.5r_{vir}$) and the onset of quenching. This is motivated by the results of Wetzel et al. (2012) who show the existence of persistent bimodality in the specific star formation distribution of galaxies regardless of the distance from the cluster centre. Similarly, in a follow up paper Wetzel et al. (2013) find that satellites exhibit a delayed then rapid quenching mechanism where satellites continue star formation until a given time after which they are quenched rapidly. Keeping these results in view, the definition of Δt_Q requires that satellites with an infall time less than Δt_Q are not affected by the cluster. The galaxies that are not already quenched and that have an infall time greater than Δt_Q are quenched by the cluster.

It is important to note that some satellites will already be quenched before infall into the cluster as a result of internal or mass quenching (Peng et al., 2010). Similarly, satellites that fall into the cluster as part of a group are also likely to experience environmental quenching due to the group before being quenched by the cluster. Keeping these two likely scenarios in mind, our model here fits for environmental quenching due to the cluster alone on top of any internal or small overdense region (such as that of a group) environmental quenching. Clearly, such satellites that are already quenched either by internal mechanisms or externally by the group environments will remain unaffected by the cluster. The inclusion of an infalling population ensures that preprocessing by previous hosts or due to internal effects is accounted for since our model is built to isolate the effects of the current host. Each PPS bin is therefore composed of active and quenched populations which depends on the infall time of the satellites and the free-parameter, Δt_Q.

A more intuitive approach to Δt_Q can be understood from this example: a $\Delta t_Q = 0$ Gyrs means that all the galaxies are quenched by the cluster as soon as they fall into it. In contrast, a $\Delta t_Q = 5$ Gyrs means that galaxies are quenched after

spending 5 Gyrs in the cluster environment. In this case, all the galaxies with an infall time less than 5 Gyrs will remain unquenched and hence their colours would be represented by the unquenched colour distribution while the ones with an infall time greater than 5 Gyrs will have their colours reddened by the amount of quenching experienced by them. For example, satellites with an infall time of 6 Gyrs would be quenched for a Gyr, and those with an infall time of 7 Gyrs would be quenched for 2 Gyrs, and so on. Thus, the colours of such quenched populations are controlled by their infall time and Δt_Q. A given PPS bin's colour distribution is thus a mixture of both a quenched and unquenched population.

We model the affect of quenching on individual satellites and fit for the time, Δt_Q, by matching the disc colour distribution from model prediction against the observations in all PPS bins simultaneously.

Below we describe how disc quenching predicts the colours of quenched populations with different infall times and the process for generating the model prediction for the disc colour distribution in a given PPS bin.

3.1 Disc fading and reddening for quenched population

In this section, we describe on how colour distributions for the quenched populations are obtained from Stellar Population Synthesis (SPS) models. Since a given PPS bin includes galaxies having fallen in at different times, these galaxies are thus quenched by the cluster by varying amounts. We assume that all satellites start their star formation at the same redshift, $z_f = 2.5$ (2.2 Gyrs since Big Bang), are truncated at different times based on their infall times and recorded at $z_{Obs} = 0.07$ (median redshift of data). This truncation is applied as a sharp cut off to an exponentially declining star formation history (see Fig. 3.1) which leads to a fading in luminosity as shown in Fig. 3.1 bottom panel by an amount L_Q/L_A (see Eq. 3.1).

To obtain luminosities and colours of active and quenched populations, we employ the *EzGal* (Mancone and Gonzalez, 2012) package that, given an arbitrary stellar population synthesis (SPS) model, outputs observable parameters such as magnitudes, colours and mass-to-light ratios. The package allows us to choose a star formation history (SFH), z_f, metallicity (Z = 0.0125; see Appendix C on how we determine the average stellar metallicity for our sample) and an SPS model. For our purpose, we choose an exponentially declining dust-free star formation history for all galaxies in our sample, and the (Bruzual and Charlot, 2003, hereafter BC03) SPS model that uses a Chabrier (2003) initial mass function. For this choice of z_f and SPS model along with a range of characteristic e-folding times, τ, for the exponentially declining SFH, we generate g and *r-band* magnitudes and mass-to-light

ratios. This provides a relation between the $g - -r$ colour and τ's. We interpolate this relationship to allot τ values to our input galaxies based on their colours. The input galaxies are the infalling population that have not fallen into the cluster yet and hence are unaffected by its environment. This exercise gives us τ's for the active population. It is noteworthy that the τ value changes based on metallicity and inclusion of dust (see Sec. 3.3.2).

Once we have the star formation histories (τ's), we can then obtain colours for the quenched population via a simple 2D interpolation between τ's and infall times of populations. The colours of the quenched population are obtained from a truncated SFH where a sharp cut off at a given star formation truncation time (the time at which the SFH is cut off after its start at z_f, SF-TT) is applied to it, with the observables recorded at z_{Obs}. The next step is to fade the disc colour based on the infall time. This is done by applying fading based on mass-to-light ratios obtained for the quenched populations as follows:

$$m_{d,faded} = -2.5log\frac{L_Q}{L_A} + m_{d,int} \tag{3.1}$$

where $m_{d,int}$ is the disc magnitude of the active population and $m_{d,faded}$ is the magnitude of the faded disc. L_Q is the luminosity of the satellite truncated at SF-TT (the quenched satellite) and L_A is the luminosity of active satellite. Since disc fading can cause a satellite to fall below the detection limit. Galaxies fainter than the SDSS limit ($m_r \leq 17.77$) are removed. We note that this has a very negligible effect on the faded disc colour distribution predicted by the model.

Using the disc colour distribution from the infalling population for the active and the faded disc colour distribution of satellites for the quenched populations, we can now predict the PDF for disc colours in a given PPS bin. As mentioned earlier, a given PPS bin includes quenched as well as active populations controlled by the free parameter Δt_Q. We fit for Δt_Q by minimum χ^2 based on a simplified metric from each PPS bin. The disc colour distribution in a given PPS bin is split into two bins: blue (g–$r < 0.5$) and red (g–$r > 0.5$) shown by the green vertical hatched lines in Fig. 3.2 and the fraction of galaxies falling on each side is calculated giving blue and red fractions, f_{Blue} and f_{Red} respectively. We compare f_{Blue} from our predictions to that of the observations in each PPS bin to obtain the best fit Δt_Q corresponding to the least χ^2. The reason for the simplified χ^2 metric is that the model predictions produce an offset in the peak at the red end of the virialized population (see virialized population in Fig. 3.2). There is known to be a small issue with SPS models in that the synthetic g–r colours for old, metal rich galaxies are redder by 0.1 mag (Conroy et al., 2009; Maraston et al., 2009; Eisenstein et al., 2001). Another reason for the split is that the distribution of observed colours in the red peak has a breadth to it that is missing in our predictions. This breadth is due to a range of z_f, Z, and SFH that are likely to occur in reality, whereas we have considered only a single value of each parameter to represent the entire population.

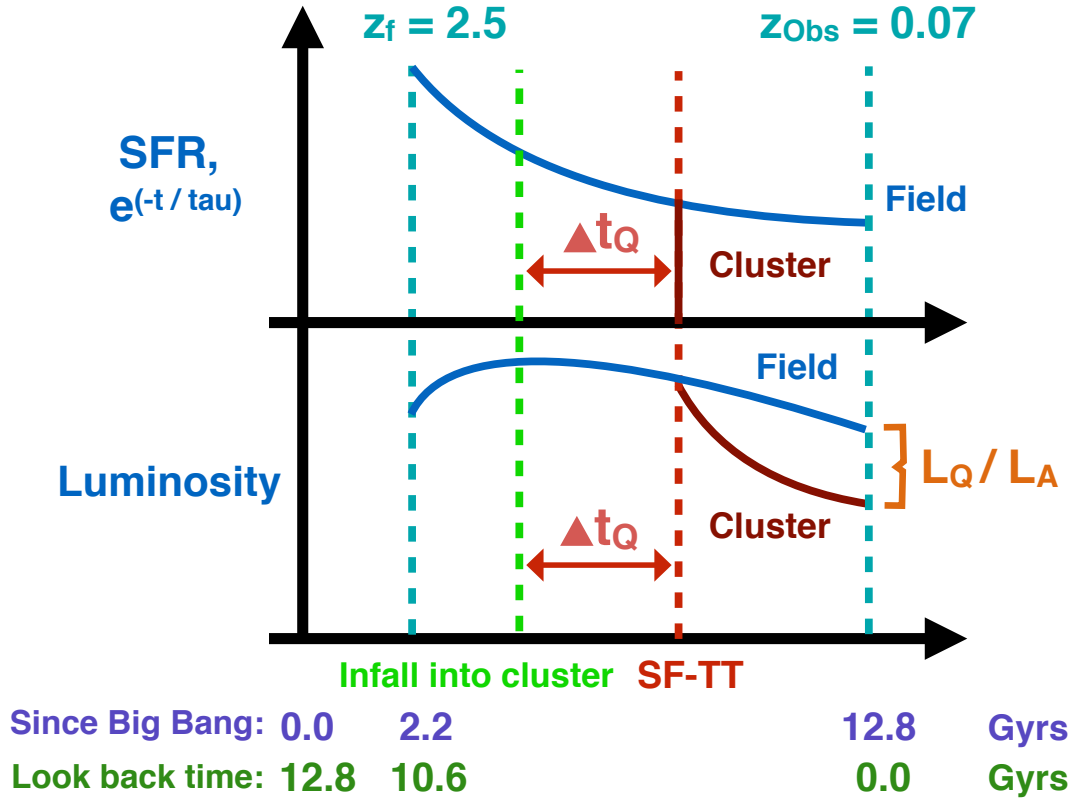

Figure 3.1: Top panel: Schematic showing an exponentially declining star formation rate (SFR) starting at formation redshift, z_f and observed at the median redshift of the data, $z_{Obs} = 0.07$. The blue curve shows untruncated SFR for a field galaxy or the one unaffected by the cluster while the SFR for the satellite under the influence of cluster is shown by the maroon break at red hatched line. This break occurs at at time Δt_Q since infall. Bottom panel: The luminosity of an untruncated (shown in blue) and a truncated SFH (shown in blue until the star formation truncation time, SF-TT, and maroon after) is demonstrated. A satellite with truncated SFR experiences a fading by $\frac{L_Q}{L_A}$ as shown in orange. Here L_Q is the luminosity of a satellites with SFR truncated at SF-TT and L_A is the luminosity of an active/field satellite both observed at z_{Obs}.

With a simple red/blue classification, we not only reduce the effects of our restricted SPS model choice but also the factors that are difficult to control.

3.2 Disc Quenching Results

Fig. 3.2 shows the predicted as well as observed disc colour distribution for all PPS bins corresponding to the minimum χ^2. The virialized population shows a clear peak on the f_{Red} side. We have already mentioned the reason for the small offset in the peak in Sec. 3.1.

A summary of our results for the different PPS binning with no mass cuts is shown in Tab. 3.1.

3.2.1 Host and Satellite Mass cuts

Previous work (Wetzel et al. (2013); Oman and Hudson (2016)) has explored the dependence of quenching on host and satellites masses. In order to check for host and satellite dependence, we subdivide our sample by host mass cut as well as by satellite mass. The host mass binning is: low-host-mass (LHM), $10^{13} < M_{halo} < 10^{14} M_{\odot}$ and high-host-mass (HHM), $10^{14} < M_{halo} < 10^{15} M_{\odot}$, bins. Each of these host-mass bins are further split into two satellite mass bins: low-sat-mass (LSM), $10^{10.3} < M_{sat} < 10^{10.6} M_{\odot}$, and high-sat-mass (HSM), $10^{10.6} < M_{sat} < 10^{12} M_{\odot}$. The satellite mass splitting is based on the median masses of the satellite mass distribution in our sample, which is $10^{10.6} M_{\odot}$.

In Tab. 3.2, we show our results for different host and satellite mass cuts as well as different choice of PPS binning (see Sec. 2.5). Note that the definition of infalling and virialized population is the same as mentioned in Sec. 2.4 and 2.5 (for different PPS binning). For a given PPS binning scheme, e.g., *Extended*, we find that the quenching time, Δt_Q, varies over 2 Gyrs. This is larger than the error estimate in Δt_Q which suggests that the trends are real. In general, we find LSM to be more resistant to quenching, similar to previous findings (see Sec. 3.4). There is also a trend in HHM where satellites take longer to quench in massive host environments.

3.3 Discussion of systematics

Different systematics contribute to the error estimation. In this section, we look at two possible systematics that could affect our results.

PPS binning	Δt_Q (Gyrs)	Δt_{ST} (Gyrs)	Δt_{MT} B/T cut = 0.1 (Gyrs)	$\Delta t_{MT,m}$ B/T cut = 0.1 (Gyrs)	Δt_{MT} B/T cut = 0.3 (Gyrs)	$\Delta t_{MT,m}$ B/T cut = 0.3 (Gyrs)
Extended	5.1	4.8	5.51 ± 0.20	4.88 ± 0.27	7.38 ± 0.60	7.61 ± 0.71
Restricted	5.6	4.8	5.55 ± 0.20	5.10 ± 0.26	6.96 ± 0.38	7.19 ± 0.61
Diagonal	4.8	5.1	5.58 ± 0.15	4.90 ± 0.22	6.95 ± 0.22	7.31 ± 0.47
Equal Number	5.4	4.8	5.58 ± 0.20	5.04 ± 0.26	7.26 ± 0.59	7.42 ± 0.65

Table 3.1: Summary of results for the case of no mass cuts on different PPS binnings. We show the disc quenching time, Δt_Q; the disc stunting time Δt_{ST}; the morphological transformation time using processed discs, Δt_{TM} (for both B/T cuts of 0.1 and 0.3) and morphological transformation with B/T in mass, $\Delta t_{MT,m}$.

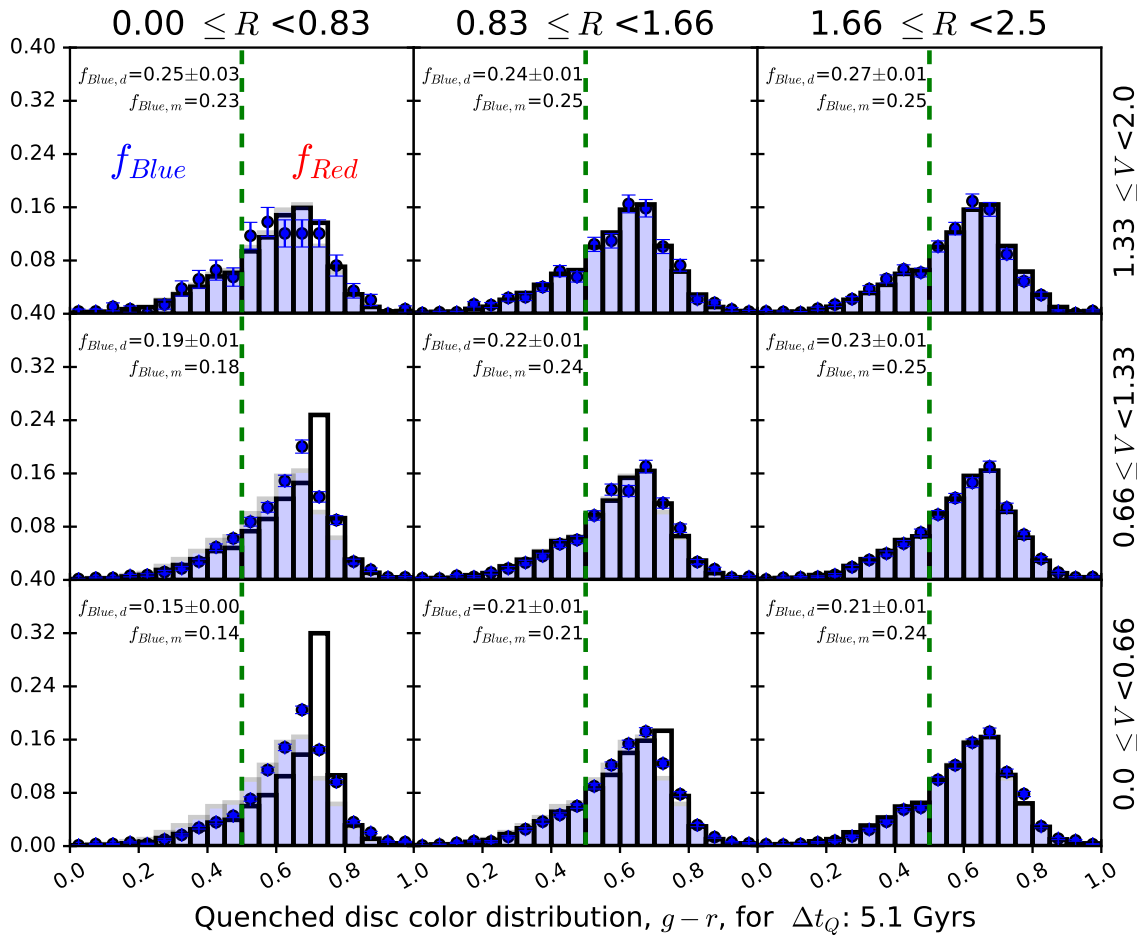

Figure 3.2: g–r disc colour PDF from the predictions is shown by the black solid histogram and observations in blue points for the least χ^2 fit corresponding to Δt_Q = 5.1 ± 0.5 Gyrs. These results correspond to *Extended* PPS binning with no mass cuts. Light blue shaded distribution is the same in all bins which is a representation of the colour distribution for the infalling population for reference. Each bin shows the blue fraction in the model and data printed as f_{Blue_m} and f_{Blue_d} respectively.

PPS binning	Extended	Restricted	Diagonal	Equal Number
Host, Satellite Mass Cuts				
LHM, LSM	5.4	5.6	5.1	5.4
LHM, HSM	4.5	5.1	3.9	5.4
HHM, LSM	6.5	6.8	6.2	6.8
HHM, HSM	4.8	5.4	4.5	5.1

Table 3.2: Delay in quenching time, Δt_Q, for satellites with different PPS binning along with host and satellite mass cuts as defined in Sec. 3.2.1. Error estimates on all the numbers listed is ~ 0.5 Gyrs (see Sec. 3.3).

3.3.1 Choice of PPS binning

We consider the choice of different PPS binning in contribution to the error estimate for Δt_Q. In this case, Δt_Q varies over a range of 0.8 Gyrs (see Tab. 3.1) over different PPS binnings. The error contribution from different PPS-binning is assumed to be half of the range, i.e., 0.4 Gyrs.

3.3.2 Choice of SPS models

In order to see how different combinations of SPS models affect our results, we try different parameters and models. Our parameter choices include z_f: 2.0, 2.5 and 3.0, and three different SPS models: Bruzual and Charlot (2003)(hereafter BC03), Charlot and Bruzual (2007)(hereafter CB07) and Conroy et al. (2009)(herafter C09). All the models were run with a Chabrier (2003) initial mass function and an exponentially declining dust-free star formation history. Out of the nine different combinations, we chose $z_f = 2.5$ and SPS model of BC03 for the reason that in addition to corresponding to the least χ^2 (based on comparing the entire disc colour distribution for all PPS bins as oppose to the simple f_{Blue} metric) fit to the data overall, this model was also in better agreement with the observed red peak in $g--r$ (see Sec. 3.2).

To estimate the contributions to the systematic error from the SPS models we consider both the choice of an SPS model as well as the variation in z_f. For a given z_f, the average difference in Δt_Q for different SPS models is 0.4 Gyrs, the error contribution is half of this value, thus it is 0.2 Gyrs. On the other hand, for a given SPS model, the average difference in Δt_Q for different z_f is also 0.4 Gyrs, thus again, the error contribution from z_f variation is 0.2 Gyrs. Adding the error in quadrature, the error from the choice of SPS models and z_f becomes 0.3 Gyrs. Thus, considering the error from the SPS choice and the PPS binning (0.4 Gyrs), the final systematic error comes out to be ~ 0.5 Gyrs.

It is worth while to mention that other factors such as the choice of metallicity

as well as dust could also contribute to the error. As mentioned in Appendix C, we calculate the metallicity of the infalling population to be Z = 0.0125 for data without applying the mass cut to match orbital libraries, i.e., the metallicity calculation is based on 47, 757 satellites. When we apply the mass cut to match with orbital libraries and recalculate the average metallicity (for 30, 682 satellites) again following the same procedure mentioned in Appendix C, it comes to be 0.016. This is a reasonable number since with the mass cut of orbital libraries, we remove low mass satellites and are left with high mass satellites only and hence the average metallicity becomes higher. When we run our choice of *Ezgal* model: BC03 with $z_f = 2.5$ and Z = 0.016, we find an increase in Δt_Q by 0.3 Gyrs (accommodated within the error estimate) along with a shift in the red peak for the virialized population from $0.7 - 0.75$ to $0.75 - 0.8$ i.e., the predicted colours of satellites becomes redder. Furthermore, our modelling is dust free. Modelling including the effects of dust is complicated for two reasons. First, it is difficult to estimate the amount of dust. Second, if quenching is due to, for example, ram-pressure stripping, one would have to estimate the amount of dust that is stripped. However, we will show in Sec. 3.4 below that the agreement with Oman and Hudson (2016) results which is based on spectroscopic indicators of star formation, suggests that the effect of dust is not very larger.

3.4 Comparison with other works

We first compare our timescales with those by Oman and Hudson (2016) (hereafter O16) with whom we share the orbital libraries as well as the data set with. O16 use specific star formation rate as a metric for defining their active and passive satellites in contrast to *g*–*r* colour used here.

As in O16, we split satellites into two host mass bins but in contrast to them, our satellites are only divided into two mass bins. Thus, we can compare our LSM bin: $10^{10.3} < M_{sat} < 10^{10.6} M_{\odot}$ with their $10^{10.0} < M_{sat} < 10^{10.5} M_{\odot}$ bin, and our HSM bin: $10^{10.6} < M_{sat} < 10^{12.2} M_{\odot}$ with their results from $10^{10.5} < M_{sat} < 10^{11} M_{\odot}$. We don't consider their most massive bin for the reason that it has extremely few objects.

A summary of our results along with O16 is shown in Fig. 3.3. Here we compare the quenching timescales (red points, our work) with theirs (magenta). We notice that our results agree with theirs in that they follow similar trends in both host and satellite mass [1]. With regards to cuts in host mass binning, it can be seen that in either one of the methods, the high host quenching time is longer than low host

[1]Note that due to the choice of our satellite mass binned into two bins, the trends in satellite mass for O16 are not explicit but they are more obvious when taken the entire mass range ($10^9 - 10^{12} M$ in O16) into account

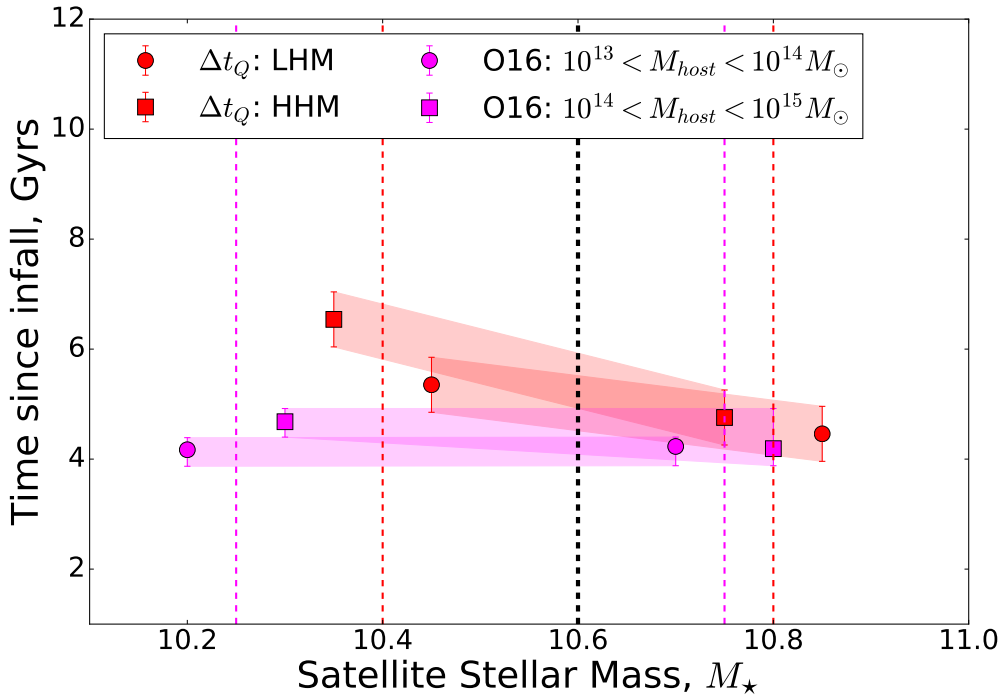

Figure 3.3: Comparison of quenching time from this work (red) and O16 (magenta). The black hatched line is drawn to separate out low satellite mass (LSM: $10^{10.3} < M_{sat} < 10^{10.6} M_\odot$) and high satellite mass (HSM: $10^{10.6} < M_{sat} < 10^{12.2} M_\odot$) for our work. The red and magenta hatched lines represent the middle of the range for both our work and O16. The data points are displaced by 0.05 dex about the median.

mass. Our results also agree with regards to satellite masses where high stellar mass satellites quench faster and low stellar mass are more resistant to quenching. Since, we only split satellites into two mass bins, we can't make any strong conclusive statements regarding the general mass trends for Δt_Q.

Moreover, comparing our results with those of Wetzel et al. (2013) (not shown here), we again find that our mass trends are shallower but nonetheless the general trend of faster quenching for massive satellites is common.

Chapter 4

Disc Size Reduction

Since the disc luminosity and hence the B/T, is also affected by disc scale length, it is interesting to compare the median disc scale lengths between the infalling and the virialized populations. We find a reduction by $\sim 5\%$ with virialized discs being smaller. We imagine two possible scenarios that could lead to a smaller disc size in the virialized population. First, it is possible that satellites within the cluster experience processes such as differential fading/quenching and/or tidal stripping that remove disc mass rendering it smaller in size. Second, there is also a possibility that satellites after infall into the cluster do not grow, where their field counterparts do. Several authors (Bruce et al., 2014; van der Wel et al., 2014) have shown that disc and bulges show a size evolution over a range of redshift such that the disc and bulge sizes grow with time with bulge sizes showing a stronger evolution compared to discs. In our model, we consider the second possibility where we have assumed that the disc scale length growth is inhibited after infall into the cluster compared to the field galaxies (hereafter 'disc stunting'). We clarify here that the chosen interpretation does not have any effect on our treatment of the model, since either interpretation leads to smaller discs which reduces the disc luminosity and will affect B/T.

4.1 Modelling

In this model, we fit for a disc scale length stunting time, Δt_{ST}, by comparing the model prediction of disc scale length with that from observations. Discs with an infall time less than Δt_{ST} continue to grow within the cluster similar to their field counterparts and hence their sizes resemble those of the infalling population, while those with an infall time greater than Δt_{ST} are affected by the cluster based on their infall time. For example, if $\Delta t_{ST} = 0$ Gyrs, the disc sizes of populations that fell in the cluster at different infall times will resemble the disc sizes of field galaxies at the

PPS binning	Extended	Restricted	Diagonal	Equal Number
Host, Satellite Mass Cuts				
LHM, LSM	6.0	5.1	5.7	6.0
LHM, HSM	5.7	5.1	5.1	5.1
HHM, LSM	6.8	6.5	6.2	6.5
HHM, HSM	4.5	4.5	5.1	4.5

Table 4.1: Delay in stunting time, Δt_{ST}, with different PPS binning and host and satellite mass cuts as defined in Sec. 3.2.1. Error estimate on all the numbers listed is 0.15 Gyrs (see Sec. 4.3).

time that they fell in i.e., they didn't grow like their field counterparts as soon as they fell into the cluster. In other words, their disc sizes were frozen at the moment they joined the cluster. Similarly, if $\Delta t_{ST} = 5$ Gyrs, satellites with infall time < 5 Gyrs will have the same disc scale length as the infalling population while satellite with infall time > 5 Gyrs will have their disc sizes reduced based on their infall time. For example, a satellite with an infall time of 6 Gyrs would have a disc scale length corresponding to a field galaxy a Gyr before z_{Obs}. This satellite kept growing like its field counterpart until 5 Gyrs since infall after which it didn't grow for a Gyr so its size is similar to a field galaxy a Gyr ago from z_{Obs}. To obtain the appropriate disc sizes for the infalling population at different infall times, we use the prescription for late-type galaxies by van der Wel et al. (2014) given as: $R_{eff} \sim (1+z)^{-0.75}$. A reduction in disc size compared to the present day galaxies in the field is thus simply: $(1+z)^{-0.75}/(1+z_{Obs})^{-0.75}$. Since this reduction would impact the disc magnitude, we apply the same methodology as with disc quenching where the discs fainter than the SDSS magnitude limit are dropped from the sample. Thus, when including both disc quenching and disc stunting in our model, more objects are dropped due to the SDSS magnitude limit but the effect is still small.

4.2 Disc Stunting Results

In Fig. 4.1, we show our results corresponding to the least χ^2 at $\Delta t_{ST} = 5.1 \pm 0.15$ Gyrs reproducing disc-scale lengths in all PPS bins based on the simple model described above. The χ^2 calculation here is based on the median of the distribution which is shown on each PPS bin.

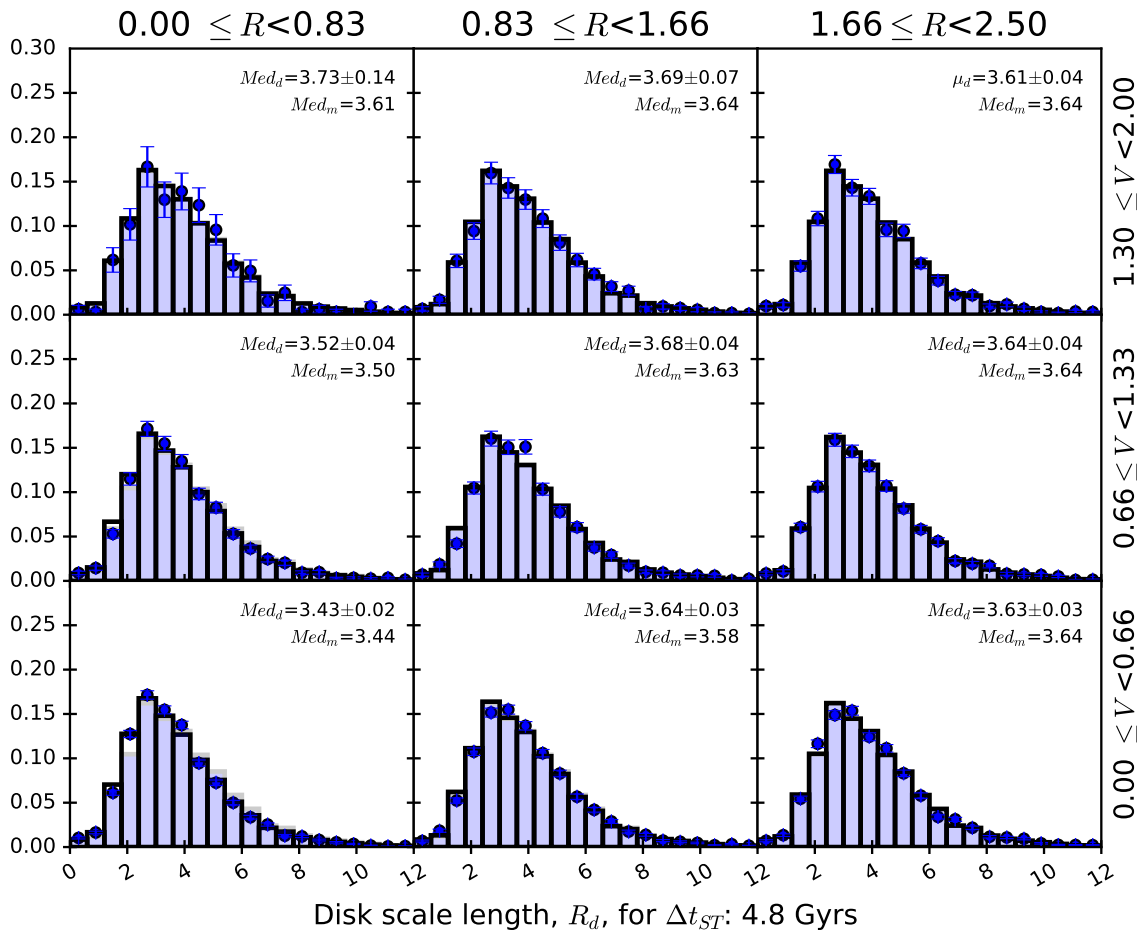

Figure 4.1: Disc scale length distribution for model in black solid histogram with blue data points and infalling population as filled histogram. The median of each distribution upon which the χ^2 is based is printed on each PPS bin.

4.3 Discussion

We first comment on the error estimate on Δt_{ST}. The error contribution comes only from PPS-binning (see Tab. 3.1) which is ~ 0.15 Gyrs.

In Tab. 4.1 we show our results for comparing Δt_{ST} for different host and satellite mass cuts as well as PPS binning. For a given choice of PPS binning, the variation in time range exceeds the error estimate and thus the trends would have to be considered real. We notice a similar trend with regards to satellite mass as with disc quenching which is that low mass satellites are more resistant to disc stunting.

A comparison between Δt_Q (5.1 ± 0.5 Gyrs) and Δt_{ST} (4.8 ± 0.15 Gyrs) shows that the two timescales are similar. This similarity suggests that the processes responsible for disc-quenching and disc stunting could occur simultaneously. In Fig. 4.2, we show a comparison of quenching time, Δt_Q, and disc stunting time, Δt_{ST} for different host and satellite mass cuts (see Sec. 3.2.1). The two timescales agree with each other within the errors further strengthening our conclusion that both quenching and disc stunting occur simultaneously.

We now comment on a possible set of mechanisms leading to a reduction in disc scale length. A disc scale length reduction could be induced due to the discs experiencing differential fading. By "differential fading" we mean that the entire disc is quenched at the same time but it fades differentially. This means that due to quenching there is a halt of star formation at all radii, but because of differential fading, there is an excess drop in surface brightness at larger radii within the galaxy leading to smaller disc scale length. A differential fading would be visible in the colour gradient of discs where the outskirts would be blue and the colour becomes redder moving inwards toward the disc centre. This essentially means that, in our model, a given disc would have a variety of τ's as a function of disc radius as opposed to the single τ as we have assumed. In our data set however, we are unable to confirm this because GIM2D fits simultaneously in both g and r-bands. The magnitude measured in these bands are thus extracted from the same disc scale length which hides any colour gradient. Despite the fact that we cannot test for the gradients, the similarity in the timescales for Δt_Q and Δt_{ST} is suggestive that differential fading could be a possible explanation for a decrease in disc scale length.

Contrary to the above proposition, a disc scale length reduction can also be caused by differential quenching (Schaefer et al., 2017). In this case, if satellites quench in an outside-in fashion where the outer wings are quenched first and the inner regions later then the surface brightness drops faster at larger galactocentric radii compared to the central disc region thus the disc scale length would be reduced. But the central surface brightness would remain the same (unlike the case of differential fading where both I_0 and R_d are effected.)

To check which one of the above two processes (differential fading or differential

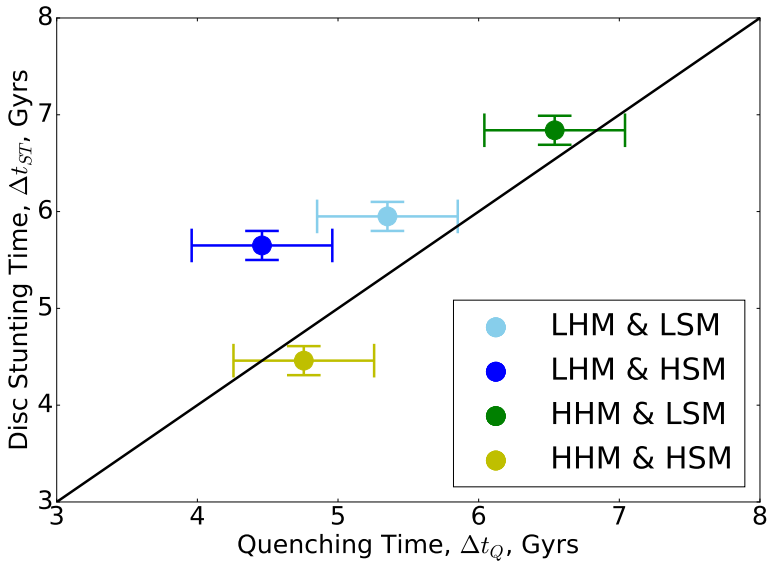

Figure 4.2: Comaprison between delay time until quenching Δt_Q and delay time until stunting, Δt_{ST} for host and satellite mass cuts mentioned in Sec. 3.2.1 for *Extended* PPS binning.

quenching) is more likely, we explore our dataset further by comparing the disc scale lengths and surface brightness for pure discs (B/T <0.1) between the infalling and the virialized populations. A comparison of the disc scale length between the two populations shows a difference of $\sim$ 10 % whereas there is no significant difference between the central surface brightnesses of the two populations (p-value = 0.5 for KS test). This result would favour the differential quenching scenario where the central surface brightness remains the same. In conclusion, our dataset in unable to distinguish between differential fading and differential quenching scenarios.

In addition to differential fading and differential quenching, processes resulting in gas supply cut off after infall into the cluster can also be responsible for a reduction in disc scale length.

Chapter 5

Morphological Transformation

So far we have modelled disc quenching and disc scale length reduction since both of them have a direct impact on disc luminosity which in return can affect the B/T. Comparing the *r-band* absolute magnitude of discs predicted by our disc quenching model in the virialized population (-20.41) to those from observation (-20.24 $\pm$ 0.01), shows that disc quenching alone is not enough in reproducing observed disc fading. When we incorporate disc stunting along with quenching requiring the satellites to be quenched at Δt_Q and stunted at Δt_{ST}, we find the predicted disc magnitude median further drops to -20.30 vs. -20.24 $\pm$ 0.01 (observation). As mentioned earlier, if the disc luminosity is reduced, this leads to a higher B/T. To compare how both quenching and stunting impact morphology, we show the B/T distribution of satellites in the virialized population affected by disc quenching (left) and disc quenching as well as stunting (right) in Fig. 5.1.

We separate the morphology into two bins: "late-type" with B/T $\leq$ 0.1 and "early-type" with B/T $>$ 0.1 as shown in Fig. 5.1 (note that this distinction between early and late-type is not the usual definition). The early-type fraction from the model and data is printed as $f_{e,m}$ and $f_{e,d}$ respectively. The left panel in Fig. 5.1 shows that quenching has a very small effect on morphology, specially visible in the $0.1 - 0.2$ bin (comparing the light blue filled histogram representative of the infalling population to the black model prediction). On the other hand, it can also be seen that the model predicts a surplus of discs in the $0.0 - 0.1$ bin. At higher B/T, the model under predicts compared to the observations but this is an expected consequence since the histogram is normalized. Similarly, the model distribution in the right panel fits the data better than before overall however, the excess of discs in $0.0 - 0.1$ bin is still present. This is because, for objects with a negligible or no bulge, a drop in disc luminosity would have no impact on their B/T as the numerator remains zero. We show the B/T distribution results for all PPS bins from *Extended* PPS binning (no mass cuts) with discs processed by quenching and stunting at their respective times in Fig. 5.2. It can be seen that disc quenching

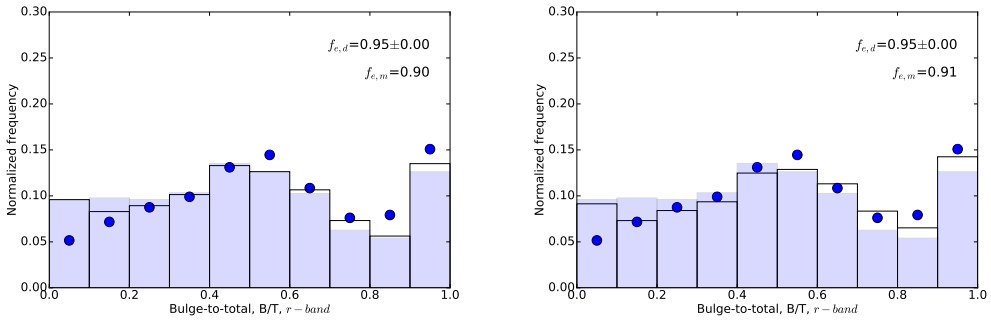

Figure 5.1: *r-band* B/T distribution for the virialized population from *Extended* PPS binning with no mass cuts. The black solid curve shows the model prediction compared with the blue data points. The filled light blue histogram is representative of the infalling population. The early-type fraction is printed as $f_{e,m}$ and $f_{e,d}$ for model and data respectively. The green hatched line is drawn at a B/T cut of 0.1 separating out the late and early-type satellites. The left panel shows the distribution by modelling disc quenching only. The right panel is shows the prediction of quenching as well as disk stunting.

and stunting have some effect on morphology but this does not entirely explain the morphological transformation specially for satellites with B/T < 0.1 in the virialized population. Other processes must be at work that could be responsible for driving late-type to early-type galaxies.

5.1 Model

In order to account for the processes that act over and above disc quenching and stunting in affecting morphology, the third part of the model accounts for the excess morphological transformation by fitting for a time, Δt_{MT}, at which the late-type satellites transform into early-type by a structural change i.e., a redistribution of stellar mass. The model predicts the total fraction of early-type galaxies in a given PPS bin. This prediction is based after the late-type galaxies processed by disc quenching and stunting at their respective times have transformed into the early-type as a function of the amount of time spent in the cluster (the infall time probability given by $P_{t-(t+1)}$) by crossing over the 0.1 threshold in B/T given by the following expression:

$$f_{e,T} = f_l \sum_{t=0}^{t=10} f_{t-(t+1)} P_{t-(t+1)} + f_e \tag{5.1}$$

The prescription above takes in fraction of processed late and early-type satel-

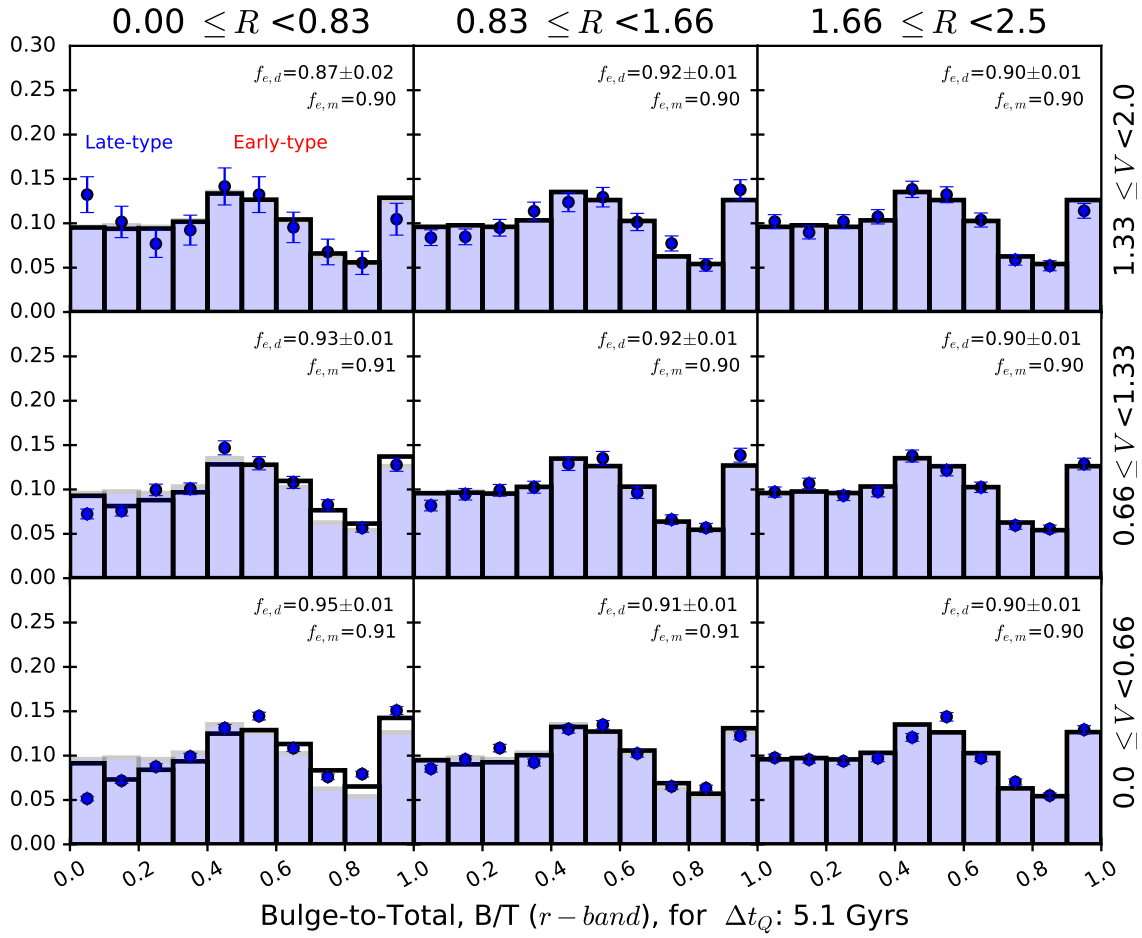

Figure 5.2: B/T distribution for *Extended* PPS binning for the case of no mass cuts with discs processed with quenching and stunting at their respective times. As before, the black solid histogram represents model prediction with blue data points and infalling population as filled histogram. Each PPS bin shows $f_{e,m}$ and $f_{e,d}$ correspnding to the early type fraction from the model and data respectively. The separation between late and early-type is based on B/T = 0.1.

lites, f_l ($= 1 - f_e$) and f_e, respectively that comes from the early-type morphology bin mentioned above. We clarify here that the word 'processed' means satellites in a given PPS bin that have been previously modelled with disc quenching and disc stunting. $f_{t-(t+1)}$ is the fraction of galaxies transformed from disc to early-type between infall time: t and $t+1$. We assume that f_t's evolve monotonically with infall time resembling an error function where we fit for μ (note that $\mu = \Delta t_{MT}$) and s as shown below:

$$f_t = \frac{1}{2} + \frac{1}{2} erf\left(\frac{(t-\mu)}{\sqrt{2}s}\right) \tag{5.2}$$

The fits from Eq. 5.2 predict f_t at a given time which is then used to evaluate the total early-type fraction, $f_{e,T}$, in a given PPS bin using Eq. 5.1. We then compare the early-type fraction from the model to the observation and reduce the χ^2.

5.2 Results: Processed f_e

We show our morphological transformation results in Fig. 5.3 showing fraction of galaxies transformed, f_t, as a function of time since crossing $2.5r_{vir}$ Gyrs. We find that the time required for the late-type fraction (already processed by disc quenching and disc stunting) to become an early-type population (i.e., cross the threshold of B/T > 0.1) is $\Delta t_{MT} = 5.51 \pm 0.20$ Gyrs. Thus, disc fading driven by quenching and stunting, occurs on similar time scales as changes in morphology. The morphological change in most satellites with a B/T > 0.1 can be explained by quenching and stunting while satellites with B/T < 0.1 are negligibly affected by these processes and are more strongly impacted by other active process that transform them into early-type systems.

We also repeat this test for different host halo mass cuts, satellite mass cuts (Sec. 3.2.1) and phase-space binning (Sec. 2.5). Table 5.1 bottom section shows a summary of our findings.

5.3 Results: f_e in stellar mass

In addition to finding a time scale for morphological transformation of satellites based on disc quenching and disc stunting, we also attempt to fit for another morphological transformation time scale, $\Delta t_{MT,m}$, based on the B/T in stellar mass from Mendel et al. (2014). This is carried out in a similar way as mentioned in section 5.1 using Eq. 5.1 and Eq. 5.2. Only that now, f_e, is not "processed" but rather is purely based on data past a cut of B/T > 0.1. This serves as an independent

PPS binning	Extended	Restricted	Diagonal	Equal Number
Host, Satellite Mass Cuts		B/T cut = 0.3		
LHM, LSM	8.61 ± 0.73	8.73 ± 0.69	8.52 ± 0.73	8.78 ± 0.71
LHM, HSM	6.27 ± 0.64	6.67 ± 0.73	7.61 ± 1.04	7.14 ± 0.89
HHM, LSM	7.28 ± 0.29	7.82 ± 0.27	8.11 ± 0.26	7.81 ± 0.28
HHM, HSM	6.64 ± 0.67	6.29 ± 0.49	5.67 ± 0.21	6.21 ± 0.47
		B/T cut = 0.1		
LHM, LSM	6.70 ± 0.52	7.11 ± 0.66	6.19 ± 0.35	6.83 ± 0.59
LHM, HSM	5.25 ± 1.29	5.88 ± 1.42	5.80 ± 1.41	6.45 ± 1.48
HHM, LSM	6.54 ± 0.18	6.56 ± 0.18	6.90 ± 0.21	6.58 ± 0.19
HHM, HSM	4.63 ± 0.42	5.24 ± 0.51	4.50 ± 0.30	5.07 ± 0.41

Table 5.1: Morphological transformation time, Δt_{MT}, for discs processed by quenching and stunting for different PPS binnings and host and satellite mass cuts with B/T = 0.3 (top) and a cut of B/T = 0.1 (bottom).

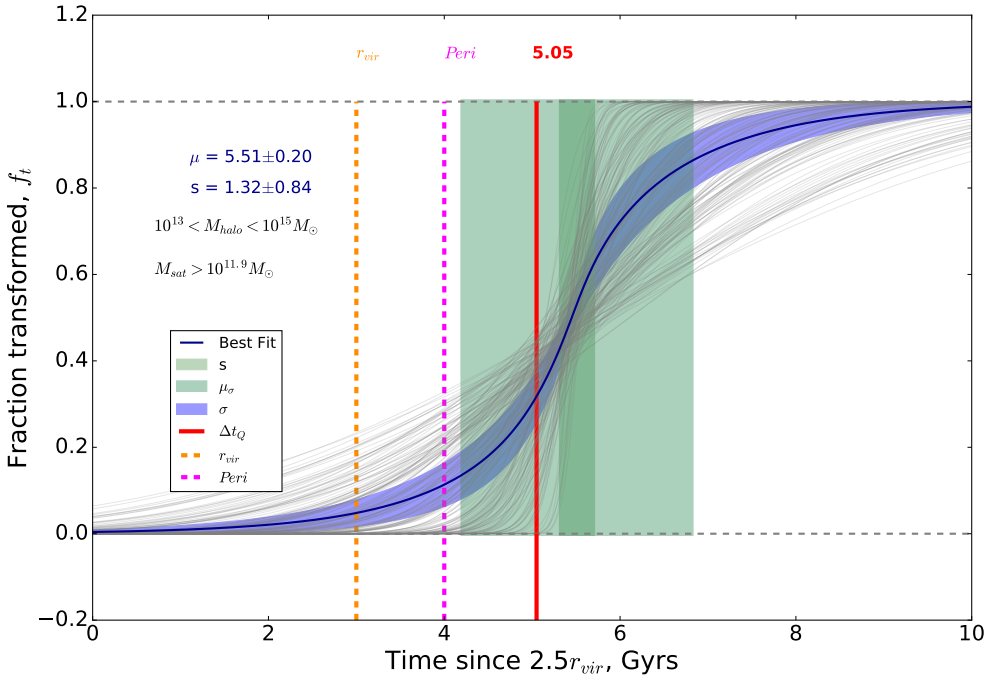

Figure 5.3: Fraction of satellites transformed from B/T < 0.1 to B/T > 0.1 as a function of the time since infall. The orange and pink vertical hatched lines are drawn at r_{vir} and pericentre crossing respectively, while the red vertical solid line represents Δt_Q which we consider to be aligned with Δt_{ST} (see Sec. 4.3). The grey curves are drawn from the burned-in and thinned out MCMC chain fitting for μ and s in Eq. 5.2 while the solid blue curve is drawn at the mean of the grey curves within a given time bin. The light blue bands are representative of the 1σ error in the mean curve. Dark green vertical band shows the 1σ statistical uncertainty in Δt_{MT}, while the light green band shows the spread in Δt_{MT} given by s. This shows that morphological transformation times are not synchronized across the cluster but vary from galaxy to galaxy.

measure of the physical transformation of satellites not expected to be affected by luminosity since quenching should not change the B/T in stellar mass. Using this approach we find a time of 4.88 $\pm$ 0.27 Gyrs. Since Δt_Q, Δt_{ST}, Δt_{MT} and $\Delta t_{MT,m}$ are all similar, it can be concluded that late-type discs (B/T < 0.1) are quenched and morphological transformed at nearly the same time.

We also repeat this test for different host and satellite mass cuts (Sec. 3.2.1) as well as PPS binning (Sec. 2.5). The bottom section of Table 5.2 summarizes our results.

5.4 Discussion

In this section, we explore different physical scenarios that can explain the morphological transformation of the excess discs (B/T < 0.1) processed by quenching and stunting in our model.

As noted before, considering only the disk quenching and stunting predictions, there is a significant deficit of discs with B/T< 0.1 of discs observed compared to the predictions of the model based on the infalling population (right panel, Fig. 5.1). This deficit of discs raises two important concerns. First, we can question whether using the infalling population as input to our model is justified. The infalling population we use in our model is taken from the circum-cluster environment at z_{Obs}. It could be possible that satellites that fell in the cluster a long time ago had a higher B/T (i.e., small disc component). To check this, we find the average redshift of the objects in the virialized population. Most of the objects in this PPS bin have an infall time of about 5 Gyrs, which corresponds to z $\sim$ 1.4. SINFONI data (Tacchella et al. (2015)) shows galaxies at higher redshift (z $\sim$ 2) are disc-dominant with only 15 % satellites in their sample having a B/T $\geq$ 0.3. Therefore, the existence of discs at high redshift is supported by SINFONI data but this is presented with the caveat that the progenitors in overdense regions at z $\sim$1.4 could have a different morphological mix.

One physical scenario that could in principle explain our results is harassment. Harassment occurs due to high speed fly-bys where a satellite feels perturbation by neighbouring satellites as well as the overall cluster potential. As mentioned by Moore et al. (1996) and Moore et al. (1998), a harassment event first drives a bar instability after the first pericentric passage. As a result the satellite become less bound leading to the formation of a flattened shape where the motion of stars are now rearranged into a random fashion. Thus, harassment could manifest itself as a galaxy being puffed up. In addition to this, the disc rearranges angular momentum which is assumed to result in funnelling either gas mass or stellar mass or a combination of both into the central regions of the galaxy from the disc. In the next few paragraphs, we explore whether harassment can explain the excess 'morphological'

PPS binning	Extended	Restricted	Diagonal	Equal Number
Host, Satellite Mass Cuts		B/T cut = 0.3		
LHM, LSM	7.95 ± 0.77	8.19 ± 0.77	7.22 ± 0.49	8.28 ± 0.77
LHM, HSM	6.65 ± 0.76	6.60 ± 0.75	7.29 ± 0.99	7.18 ± 0.97
HHM, LSM	7.52 ± 0.14	7.58 ± 0.14	7.54 ± 0.12	7.54 ± 0.18
HHM, HSM	5.82 ± 0.30	5.90 ± 0.28	5.35 ± 0.14	5.71 ± 0.24
		B/T cut = 0.1		
LHM, LSM	6.61 ± 0.82	5.45 ± 0.65	0.00 ± 0.00	5.74 ± 0.71
LHM, HSM	0.00 ± 0.00	6.73 ± 2.32	5.80 ± 1.41	0.00 ± 0.00
HHM, LSM	5.54 ± 0.33	6.08 ± 0.28	6.01 ± 0.26	5.98 ± 0.30
HHM, HSM	6.57 ± 1.45	7.14 ± 1.14	5.03 ± 0.92	6.49 ± 1.38

Table 5.2: Morphological transformation time, $\Delta t_{MT,m}$, from B/T in mass based on a cut of B/T = 0.3 (top) and a cut of B/T = 0.1 (bottom). We show results from different PPS binnings as well as host and satellite mass cuts. A value of 0.00 represents failed runs where no objects were found below B/T cut = 0.1.

transformation.

As mentioned above harassment can cause an inflow of material from the disc component of a satellite to the central region. If there is an inflow of gas, this creates a scenario where the disc is quenched due to the gas inflow towards the centre. This gas inflow could lead to a star burst event in the bulge shortly after the quenching time, Δt_Q. Thus, a small population of bulges would be expected to be blue. However, the bulge colours for the virialized population, have a smooth distribution peaking in the red region with no sign of any excess in the blue. Moreover, comparing the g–r colours of bulges in the infalling population vs. the virialized, we find that the median of the two distributions does not differ significantly. We infer from this that if harassment caused star formation in the bulge then it did not leave a detectable signature. On the contrary, if the satellite has no gas and there is an inflow of stellar mass due to harassment, this could possibly lead to a formation of bulge within an otherwise bulgeless disc. This scenario is explained by Moore et al. (1999) in their fig. 7 that shows late-type galaxies with low surface brightness being more susceptible to mass inflow. Such satellites after having spent considerable time in the cluster become faint and diffuse in their outskirts with the an increase in the central surface brightness which they attribute to harassment. This increase in central surface brightness when fit with an algorithm such as GIM2D Simard (1998), might yield a "bulge" component for such galaxies. The formation of such a bulge from central mass concentration is usually referred to as pseudo-bulge in the literature. One distinguishing feature of such bulges compared to 'classical' bulges is that the pseudo-bulges appear to have a more flatter, peanut shape. Unfortunately, our data set doesn't allow us to distinguish the bulges at this level of detail. But we can check whether mass transference from disc to bulge takes place via comparing the bulge and disc luminosities. To check this scenario, we compare the increase in bulge brightness in the virialized population with the deficit in absolute disc magnitude predicted by the first two steps of the model accounting for disc quenching and disc scale length reduction. A comparison of the median bulge luminosity between the infalling and the virialized population shows the virialized population bulges to be brighter by ~ 0.06 mag. If there is mass transference from the disc to the bulge component, the deficit in absolute disc magnitude between the model prediction and observations in the virialized population should account for it. When comparing the absolute disc magnitude from the model prediction accounting for by quenching and disc scale length reduction with the observations in the virialized population, we find a difference of ~ 0.06 mag which perfectly accounts for the increase in bulge luminosity of the virialized population. While this shows that a possible mass transference from disc to bulge took place, it also further strengthens our conclusion that an additional structural change takes place in satellites which plays its part in determining the morphology of satellites.

We can also get more insight into morphological transformation by analyzing

the results from *Diagonal* PPS binning. The B/T model prediction with discs processed by quenching and stunting for the *Diagonal* PPS binning case is shown in Fig. 5.4. The virialized population in this case (top left PPS bin) shows that for all objects with a B/T < 0.3 disc quenching and stunting is not enough to explain the morphology unlike the *Extended* PPS binning where only B/T < 0.1 objects required other processes. The prediction in B/T for the *Extended* and *Diagonal* PPS binning can be understood by comparing Fig. 2.4 and Fig. 2.2. In Fig. 2.4, the virialized population is represented by the lower left bin. If the dimensions of this bin are superimposed on top of Fig. 2.2, it would be visible that such a PPS bin becomes a pure virialized population whereas the virialized population defined in the *Extended*-PPS drawn over by white lines in Fig. 2.2 is a contaminated sample as it consists of objects with a variety of infall times. Now, if we define the late and early type morphologies based on a B/T cut of 0.3 (for *Diagonal* PPS binning) instead of 0.1 as done previously (for *Extended* PPS binning), the new finding suggests a Δt_{MT} and $\Delta t_{MT,m} \sim 7$ Gyrs (see top panels in Tab. 5.1 and 5.2). This then means, quenching and stunting take place first around ~ 5 Gyrs but in order to explain the morphological transformation of objects with $0.1 <$ B/T < 0.3, to cross over the B/T $= 0.3$ threshold and become early-type (as defined here), it takes an additional 2 Gyrs. One possible interpretation of this is that objects with a bulge component are less likely to be affected by harassment compared to objects with a pure disc component only. Moore et al. (1999) showed that harassment has a strong impact on the morphology of late-type (Sc-Sd) disc galaxies and little impact on the morphology of more compact (Sa-Sb) discs. This can be understood because the dynamical timescale is shorter for more compact objects and thus a perturbation due to harassment is responded adiabatically. In addition, compact objects have less mass past tidal radius making them less susceptible to tidal stripping or to harassment. Another possible explanation for a longer timescale for these objects could be because there is a certain percentage by which the bulge size increases as a result of harassment based on the amount of time spent in cluster. The rate of B/T growth would be approximately 0.1 in B/T per Gyr after the initial 5 Gyr. In this scenario, objects with a pure disc component only would be the first ones to show a sudden jump from B/T < 0.1 to B/T > 0.1, whereas all objects initially with B/T > 0.1 would seem to be shifted, eventually leading to a build up of objects in the last bin i.e., B/T > 0.9.

Our findings suggest that while a decrease in disc luminosity (from quenching and disc scale length reduction) can account for some morphological transformation (for satellites with $0.1 <$ B/T < 0.3), these processes certainly have less of an impact *especially* for objects with B/T <0.1. Other active processes such as harassment become significant in driving morphological transformation for B/T < 0.1 satellites. Moreover, the similarity between Δt_{MT} and $\Delta t_{MT,m}$ also shows that while gas loss processes such as ram-pressure stripping and strangulation could be at work leading to an apparent morphological transformation, there is in fact a physical transfor-

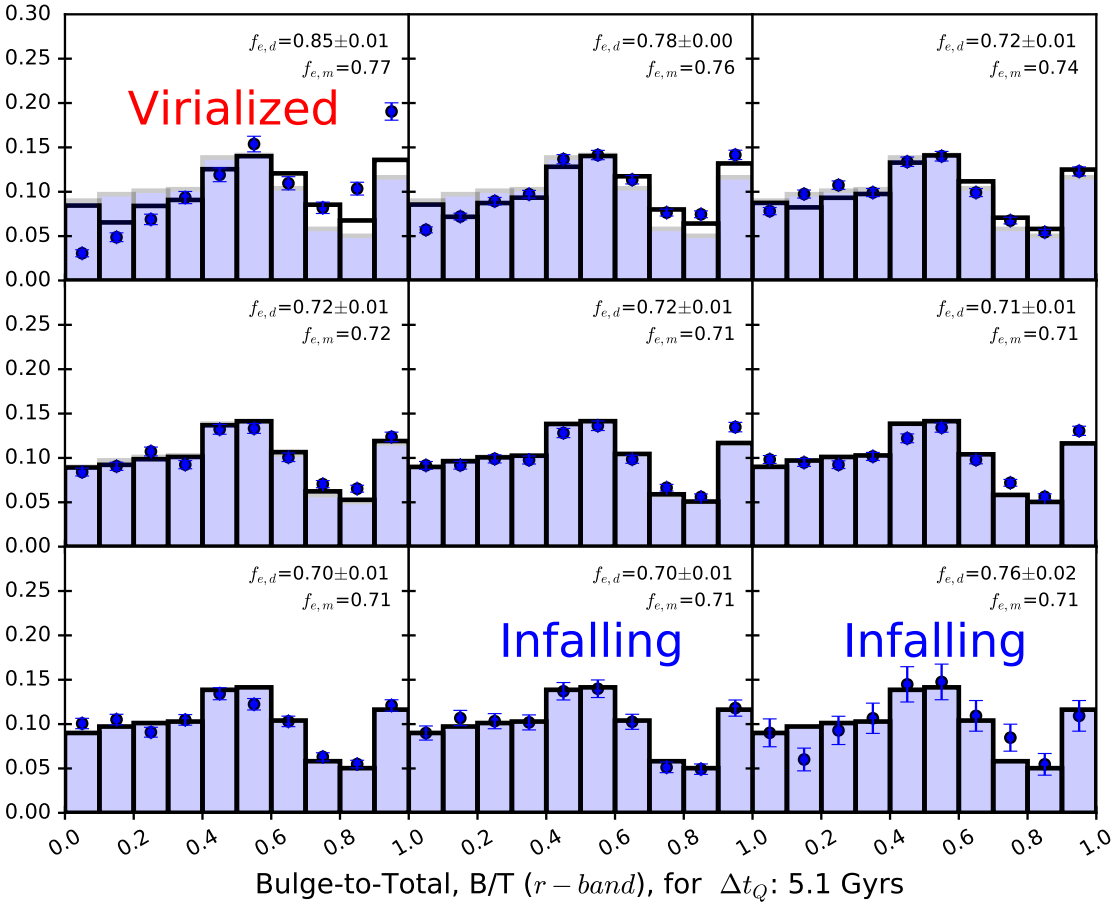

Figure 5.4: B/T distribution for *Diagonal* PPS binning for the case of no mass cuts with discs processed with quenching and stunting at their respective times. As before, the black solid histogram represents model prediction with blue data points and infalling population as filled histogram. The virialized population is represented by the top left PPS bin while the infalling population includes the second and third PPS bins in the bottom row. Each PPS bin shows $f_{e,m}$ and $f_{e,d}$ corresponding to the early type fraction from the model and data respectively. The separation between late and early-type is based on B/T = 0.3.

mation for satellites with B/T < 0.1 that occurs over the same time scale as disc quenching and stunting. Thus, the pure discs are strongly affected by the cluster environment. Similarly, we find that objects with $0.1 <$ B/T < 0.3, also require structural processes to explain their morphology if we pick out a pure virialized sample (such as that from *Diagonal* PPS binning). For such objects, in order to become an early-type satellite (i.e., cross a B/T $= 0.3$ threshold), it takes ~ 2 Gyrs longer than pure disc objects suggesting that such objects must be more resistant to a physical transformation.

We compare our conclusions with that of Carollo et al. (2016) who use ZENS data set spanning $0.05 < z < 0.0585$. They conclude that disc fading entirely is responsible for driving the density-morphology relationship. This conclusion is drawn from a comparison between satellite population at group periphery vs. the one that is within virial radius. They find that the fraction of passive early-type satellites (defined as satellites with B/T ≥ 0.5 and single component Sérsic index, $n >3$) stays constant throughout the cluster while the fraction of passive satellites increases toward cluster centre. From this result, they conclude that mass quenching and satellite quenching either have no effect or the same effect on morphology. Comparing their results with SAMs model, they find that disc fading alone can reproduce morphological transformation and that no structural transformation is induced in the satellites after infall into group environments. To draw a fair comparison with their work, we follow the same approach as theirs and compare the B/T of passive satellites (defined as $g - r$ disc color >0.5) between the infalling and virialized population for our sample. We find the medians in B/T for passive satellites to be 0.45 ± 0.01 and 0.48 ± 0.00 for infalling and virialized populations respectively. This test shows that the passive satellites have different morphology in our dataset. Moreover, we found that if we only separate satellites based on R without any separation in V, the B/T distribution medians between the outermost and the innermost R bins agree within the error bars. This shows that satellites disentanglement is strengthened by using both (R, V) coordinates and not doing so can lead to spurious conclusions where the morphological difference between the infalling and virialized populations would remain hidden. In addition to this, we also find the median bulge luminosity between our infalling and virialized population to lie outside the error in the median values showing that there is indeed a bulge "enhancement". This is in contrast to Carollo et al. (2016) who do not find any difference between the bulge luminosity between their infalling and virialized populations.

As discussed above, our conclusions suggest that a drop in disc luminosity (leading to an apparent morphological transformation) as well as structural processes are required to explain the morphology and thus they both contribute to the density-morphology relationship. Our conclusions are further strengthened by a comparison of B/T in stellar mass between infalling and virialized populations (*Extended* PPS

binning) where we find a drop of ~ 40 % for objects with B/T <0.1 (this is similar to a drop of ~ 40 % for luminous objects between infalling and virialized populations with B/T < 0.1) showing that indeed such objects are physically transformed by active processes.

In Fig. 5.5, we show a summary plot of our results for the *Diagonal* PPS bins. The vertical hatched line is drawn to separate out satellites into LSM and HSM. The square symbol shows HHM while the circles represent LHM. Focusing only on satellite mass trends alone, we find LSM are more resistant to quenching and similarly morphological transformation. On the other hand, trends based on host halo mass show some variety. HHM satellites quench on a longer time scale whereas they show a faster morphological transformation than LHM. Note that the timescales for morphological transformation: Δt_{MT} and $\Delta t_{MT,m}$ were both obtained by using a B/T cut of 0.3 as discussed above.

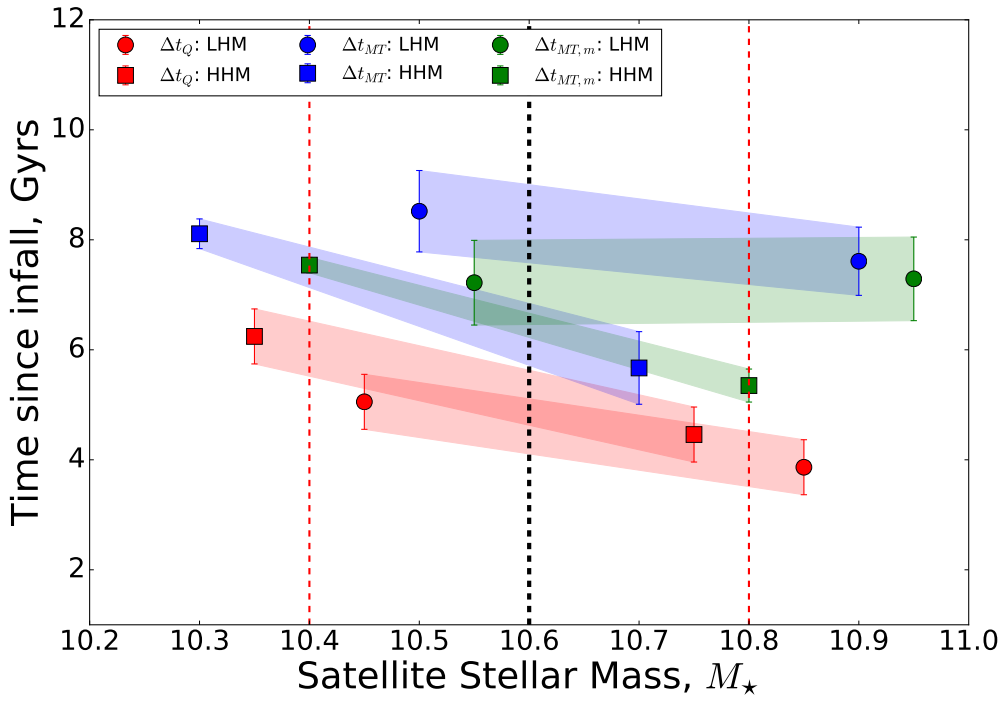

Figure 5.5: Summary of the different timescales for different mass cuts for *Diagonal* PPS binning. Red colour shows Δt_Q while blue and green represent Δt_{MT} and $\Delta t_{MT,m}$ respectively. Square data points are from low host mass cut ($10^{13} < M_{halo} < 10^{14} M_\odot$) while circle is for high host mass cut ($10^{14} < M_{halo} < 10^{15} M_\odot$). The black hatched line is drawn to separate out satellites into low ($10^{10.3} < M_{sat} < 10^{10.6} M_\odot$) and high stellar mass bins ($10^{10.6} < M_{sat} < 10^{11} M_\odot$). The results are slightly shifted along the red hatched lines representative of the median in the two satellite mass bins to avoid overlap. The morphological transformation timescales are both based on a B/T cut = 0.3.

Chapter 6

Summary & Conclusion

We have studied the evolution of satellite morphology in cluster environments using of SDSS DR7 data set employing PPS coordinates to separate out different populations of satellites that have spent varying amounts of time in the cluster environment. This is allowed by the orbital libraries of Oman et al. (2013) that provide a probabilistic mapping between the projected phase-space coordinate and the infall time into cluster marked by a crossing of 2.5 r_{vir}. We have built our model in three steps that work in succession, each targeting a different aspect of environmental measure to study its effect on morphology. The first step of our model, disc quenching, applies fading to the entire disc uniformly and predicts the time at which satellites are quenched in the cluster by matching the disc colour prediction from the model to that of the data. The second model, disc stunting, operates in a similar fashion as the first with the exception that it fits for a time scale at which disc scale lengths stop growing. Lastly, we attempt to find the time scale at which late-type satellites already processed by disc quenching and stunting models transform into early-type cluster members. Our conclusions from this study are as follows:

1. Quenching of star formation occurs shortly (1 Gyr) after crossing pericenter. In addition, quenching alone has a small effect on driving morphological transformation.

2. Disc size reduction occurs on similar time scales as quenching suggesting that the processes responsible for quenching, in addition to leading to a cessation in star formation, also leads to a reduction in disc scale length. Here the word 'reduction' is used in the comparative sense where we have assumed that the disc scale length growth is inhibited after infall into cluster compared to the field galaxies. Of course, other possibilities such as tidal mass stripping of discs is an alternative scenario for the reduced disc sizes.

3. For the case of *Extended* PPS binning, disc quenching and stunting are able

to account for morphological transformation of satellites with a B/T >0.1 but do not explain the morphology of satellites with a B/T < 0.1. This suggests that some other active processes must be involved acting over and above disc quenching and stunting that play a vital role in transforming morphology for B/T <0.1 objects.

In addition, the B/T distribution from the *Diagonal* PPS binning shows that disc quenching and stunting are both unable to explain the morphology for satellites with B/T < 0.3 suggesting that in addition to these processes, active processes equally affect B/T < 0.3 objects as well.

4. Morphological transformation fit for objects with B/T < 0.1 population gives a timescale, Δt_{MT}, (5.51 ± 0.20 Gyrs) that matches quenching (5.1 ± 0.5 Gyrs) suggesting that such satellites in addition to being affected by quenching and stunting are in fact strongly impacted by other processes such as harassment at the same time. Thus, we can conclude that objects with B/T < 0.1 (bulge-less systems) are strongly effected by cluster environment. This conclusion is strengthened when comparing the Δt_{MT} for *Diagonal* PPS binning which is ~ 2 Gyrs longer for objects with 0.1< B/T <0.3 suggesting that objects with a bulge-component are more resistant to morphological changes compared to pure discs.

5. The similarity in the timescales (Δt_Q and Δt_{MT} for pure discs) further suggest that the morphology is affected the most after the satellites pass the pericenter at which processes like ram-pressure and tidal stripping are the strongest, and satellites show the effect of the environment on morphology as early as a Gyr after crossing the densest region in the cluster.

6. Our results overall suggest that hydrodynamical and gravitational processes together are responsible for explaining the density-morphology relationship.

6.1 Future Work

In the future, we can extend the work done by identifying the bulge population of satellites that have a B/T > 0.3. Most literature mentions that pseudo bulges have a Sérsic index of ~ 1. However, it is also possible that some classical bulges have a small Sérsic index as well. On the other hand, if we assume that pseudo bulges are actually formed from the stellar disc then they should have the same metallicity as the disc component. Since bulges in general are known to have much higher metallicity, the pseudo bulges in this case would have a smaller metallicity since they are formed out of discs. There is one caveat to this scenario, and that is the mass-metallicity relationship. Less massive classical bulges would also have lower metallicity which may make it more difficult to separate the pseudo bulges from

them. Regardless, no statements can be made unless this test is actually made. In view of this, we suggest that more exhaustive studies of bulge properties (mass, size, metallicity, ellipticity etc.) be carried out as this has great potential in furthering our understanding of galactic evolution.

In addition, we suggest that more controlled N-body simulations be carried out to test the affects of harassment on a variety of satellites. These tests can include, for example, quantifying harassment incurred in a satellite with a pure disc component vs. a satellite having a disc as well as a certain percentage of bulge. This can help identify where exactly a harassed disc galaxies ends up (i.e., based on how much harassment, how does the B/T gets impacted). These simulations can be further enhanced by testing for satellites with different masses and sizes as well. Since harassment is also known to be very sensitive to the eccentricity of the orbit, a test of how these different satellites behave with respect to the eccentricity will also yield insights into how harassment plays a role in driving morphology from late to early type.

Bibliography

Abadi, M. G., B. Moore, and R. G. Bower
1999. Ram pressure stripping of spiral galaxies in clusters. *MNRAS*, 308:947–954.

Abazajian, K. N., J. K. Adelman-McCarthy, M. A. Agüeros, S. S. Allam, C. Allende Prieto, D. An, K. S. J. Anderson, S. F. Anderson, J. Annis, N. A. Bahcall, and et al.
2009. The Seventh Data Release of the Sloan Digital Sky Survey. *ApJS*, 182:543–558.

Balogh, M. L., I. K. Baldry, R. Nichol, C. Miller, R. Bower, and K. Glazebrook
2004. The Bimodal Galaxy Color Distribution: Dependence on Luminosity and Environment. *ApJL*, 615:L101–L104.

Balogh, M. L., J. F. Navarro, and S. L. Morris
2000. The Origin of Star Formation Gradients in Rich Galaxy Clusters. *ApJ*, 540:113–121.

Bell, E. F., C. Wolf, K. Meisenheimer, H.-W. Rix, A. Borch, S. Dye, M. Kleinheinrich, L. Wisotzki, and D. H. McIntosh
2004. Nearly 5000 distant early-type galaxies in combo-17: A red sequence and its evolution since z 1. *ApJ*, 608(2):752.

Bertschinger, E.
1985. Self-similar secondary infall and accretion in an Einstein-de Sitter universe. *apjs*, 58:39–65.

Bruce, V. A., J. S. Dunlop, R. J. McLure, M. Cirasuolo, F. Buitrago, R. A. A. Bowler, T. A. Targett, E. F. Bell, D. H. McIntosh, A. Dekel, S. M. Faber, H. C. Ferguson, N. A. Grogin, W. Hartley, D. D. Kocevski, A. M. Koekemoer, D. C. Koo, and E. J. McGrath
2014. The decomposed bulge and disc size-mass relations of massive galaxies at 1 z 3 in CANDELS. *MNRAS*, 444:1660–1673.

Bruzual, G. and S. Charlot
2003. Stellar population synthesis at the resolution of 2003. *mnras*, 344:1000–1028.

Butcher, H. and A. Oemler, Jr.
1978. The evolution of galaxies in clusters. I - ISIT photometry of C1 0024+1654 and 3C 295. *ApJ*, 219:18–30.

Carollo, C. M., A. Cibinel, S. J. Lilly, A. Pipino, S. Bonoli, A. Finoguenov, F. Miniati, P. Norberg, and J. D. Silverman
2016. ZENS. IV. Similar Morphological Changes Associated with Mass Quenching and Environment Quenching and the Relative Importance of Bulge Growth versus the Fading of Disks*. *ApJ*, 818:180.

Chabrier, G.
2003. Galactic Stellar and Substellar Initial Mass Function. *pasp*, 115:763–795.

Charlot, S. and G. Bruzual
2007. Updated bc03 model. *Not Published*.

Chung, A., J. H. van Gorkom, J. D. P. Kenney, and B. Vollmer
2007. Virgo Galaxies with Long One-sided H I Tails. *ApJL*, 659:L115–L119.

Conroy, C., J. E. Gunn, and M. White
2009. The Propagation of Uncertainties in Stellar Population Synthesis Modeling. I. The Relevance of Uncertain Aspects of Stellar Evolution and the Initial Mass Function to the Derived Physical Properties of Galaxies. *ApJ*, 699:486–506.

Cortese, L., D. Marcillac, J. Richard, H. Bravo-Alfaro, J.-P. Kneib, G. Rieke, G. Covone, E. Egami, J. Rigby, O. Czoske, and J. Davies
2007. The Strong Transformation of Spiral Galaxies Infalling into Massive Clusters at z˜ 0.2. In *Galaxy Evolution across the Hubble Time*, F. Combes and J. Palouš, eds., volume 235 of *IAU Symposium*, Pp. 198–198.

Cox, T. J., P. Jonsson, J. R. Primack, and R. S. Somerville
2006. Feedback in simulations of disc-galaxy major mergers. *MNRAS*, 373:1013–1038.

Croton, D. J., V. Springel, S. D. M. White, G. De Lucia, C. S. Frenk, L. Gao, A. Jenkins, G. Kauffmann, J. F. Navarro, and N. Yoshida
2006. The many lives of active galactic nuclei: cooling flows, black holes and the luminosities and colours of galaxies. *MNRAS*, 365:11–28.

Damjanov, I., P. J. McCarthy, R. G. Abraham, K. Glazebrook, H. Yan, E. Mentuch, D. Le Borgne, S. Savaglio, D. Crampton, R. Murowinski, S. Juneau, R. G. Carlberg, I. Jørgensen, K. Roth, H.-W. Chen, and R. O. Marzke
2009. Red Nuggets at z ˜ 1.5: Compact Passive Galaxies and the Formation of the Kormendy Relation. *ApJ*, 695:101–115.

de Vaucouleurs, G.
1961. Integrated Colors of Bright Galaxies in the u, b, V System. *ApJS*, 5:233.

Dekel, A. and J. Silk
1986. The origin of dwarf galaxies, cold dark matter, and biased galaxy formation. *ApJ*, 303:39–55.

Dressler, A.
1980. Galaxy morphology in rich clusters - Implications for the formation and evolution of galaxies. *ApJ*, 236:351–365.

Driver, S. P., P. D. Allen, A. W. Graham, E. Cameron, J. Liske, S. C. Ellis, N. J. G. Cross, R. De Propris, S. Phillipps, and W. J. Couch
2006. The Millennium Galaxy Catalogue: morphological classification and bimodality in the colour-concentration plane. *MNRAS*, 368:414–434.

Ebeling, H., L. N. Stephenson, and A. C. Edge
2014. Jellyfish: Evidence of Extreme Ram-pressure Stripping in Massive Galaxy Clusters. *ApJL*, 781:L40.

Eisenstein, D. J., J. Annis, J. E. Gunn, A. S. Szalay, A. J. Connolly, R. C. Nichol, N. A. Bahcall, M. Bernardi, S. Burles, F. J. Castander, M. Fukugita, D. W. Hogg, Ž. Ivezić, G. R. Knapp, R. H. Lupton, V. Narayanan, M. Postman, D. E. Reichart, M. Richmond, D. P. Schneider, D. J. Schlegel, M. A. Strauss, M. SubbaRao, D. L. Tucker, D. Vanden Berk, M. S. Vogeley, D. H. Weinberg, and B. Yanny
2001. Spectroscopic Target Selection for the Sloan Digital Sky Survey: The Luminous Red Galaxy Sample. *AJ*, 122:2267–2280.

Farouki, R. and S. L. Shapiro
1981. Computer simulations of environmental influences on galaxy evolution in dense clusters. II - Rapid tidal encounters. *ApJ*, 243:32–41.

Font, A. S., R. G. Bower, I. G. McCarthy, A. J. Benson, C. S. Frenk, J. C. Helly, C. G. Lacey, C. M. Baugh, and S. Cole
2008. The colours of satellite galaxies in groups and clusters. *MNRAS*, 389:1619–1629.

Gill, S. P. D., A. Knebe, and B. K. Gibson
2005. The evolution of substructure - III. The outskirts of clusters. *MNRAS*, 356:1327–1332.

Gunn, J. E. and J. R. Gott, III
1972. On the Infall of Matter Into Clusters of Galaxies and Some Effects on Their Evolution. *ApJ*, 176:1.

Hausman, M. A. and J. P. Ostriker
1978. Galactic cannibalism. III - The morphological evolution of galaxies and clusters. *ApJ*, 224:320–336.

Hogg, D. W., M. R. Blanton, J. Brinchmann, D. J. Eisenstein, D. J. Schlegel, J. E. Gunn, T. A. McKay, H.-W. Rix, N. A. Bahcall, J. Brinkmann, and A. Meiksin
2004. The Dependence on Environment of the Color-Magnitude Relation of Galaxies. *apjl*, 601:L29–L32.

Hubble, E. P.
1926. Extragalactic nebulae. *ApJ*, 64.

Hudson, M. J., B. R. Gillis, J. Coupon, H. Hildebrandt, T. Erben, C. Heymans, H. Hoekstra, T. D. Kitching, Y. Mellier, L. Miller, L. Van Waerbeke, C. Bonnett, L. Fu, K. Kuijken, B. Rowe, T. Schrabback, E. Semboloni, E. van Uitert, and M. Velander
2015. CFHTLenS: co-evolution of galaxies and their dark matter haloes. *MNRAS*, 447:298–314.

Hudson, M. J., J. B. Stevenson, R. J. Smith, G. A. Wegner, J. R. Lucey, and L. Simard
2010. Colours of bulges and discs within galaxy clusters and the signature of disc fading on infall. *MNRAS*, 409:405–420.

Jáchym, P., J. Palouš, J. Köppen, and F. Combes
2007. Gas stripping in galaxy clusters: a new SPH simulation approach. *aap*, 472:5–20.

Kenney, J. D. P., M. Geha, P. Jáchym, H. H. Crowl, W. Dague, A. Chung, J. van Gorkom, and B. Vollmer
2014. Transformation of a Virgo Cluster Dwarf Irregular Galaxy by Ram Pressure Stripping: IC3418 and Its Fireballs. *ApJ*, 780:119.

Kitzbichler, M. G. and S. D. M. White
2008. A calibration of the relation between the abundance of close galaxy pairs and the rate of galaxy mergers. *MNRAS*, 391:1489–1498.

Klypin, A., A. V. Kravtsov, O. Valenzuela, and F. Prada
1999. Where Are the Missing Galactic Satellites? *ApJ*, 522:82–92.

Larson, R. B., B. M. Tinsley, and C. N. Caldwell
1980. The evolution of disk galaxies and the origin of S0 galaxies. *ApJ*, 237:692–707.

Mahajan, S., G. A. Mamon, and S. Raychaudhury
2011. The velocity modulation of galaxy properties in and near clusters: quantifying the decrease in star formation in backsplash galaxies. *MNRAS*, 416:2882–2902.

Mancone, C. and A. Gonzalez
2012. EzGal: A Flexible Interface for Stellar Population Synthesis Models.

Maraston, C., G. Strömbäck, D. Thomas, D. A. Wake, and R. C. Nichol
2009. Modelling the colour evolution of luminous red galaxies - improvements with empirical stellar spectra. *MNRAS*, 394:L107–L111.

Mayer, L., C. Mastropietro, J. Wadsley, J. Stadel, and B. Moore
2006. Simultaneous ram pressure and tidal stripping; how dwarf spheroidals lost their gas. *MNRAS*, 369:1021–1038.

McCarthy, I. G., C. S. Frenk, A. S. Font, C. G. Lacey, R. G. Bower, N. L. Mitchell, M. L. Balogh, and T. Theuns
2008. Ram pressure stripping the hot gaseous haloes of galaxies in groups and clusters. *MNRAS*, 383:593–605.

McNamara, B. R., D. A. Rafferty, L. Bîrzan, J. Steiner, M. W. Wise, P. E. J. Nulsen, C. L. Carilli, R. Ryan, and M. Sharma
2006. The Starburst in the Abell 1835 Cluster Central Galaxy: A Case Study of Galaxy Formation Regulated by an Outburst from a Supermassive Black Hole. *ApJ*, 648:164–175.

Mendel, J. T., L. Simard, M. Palmer, S. L. Ellison, and D. R. Patton
2014. A Catalog of Bulge, Disk, and Total Stellar Mass Estimates for the Sloan Digital Sky Survey. *ApJS*, 210:3.

Mo, H., F. C. van den Bosch, and S. White
2010. *Galaxy Formation and Evolution*. Cambridge University Press.

Moore, B., N. Katz, G. Lake, A. Dressler, and A. Oemler
1996. Galaxy harassment and the evolution of clusters of galaxies. *nat*, 379:613–616.

Moore, B., G. Lake, and N. Katz
1998. Morphological Transformation from Galaxy Harassment. *ApJ*, 495:139–151.

Moore, B., G. Lake, T. Quinn, and J. Stadel
1999. On the survival and destruction of spiral galaxies in clusters. *MNRAS*, 304:465–474.

Oman, K. A. and M. J. Hudson
2016. Satellite quenching time-scales in clusters from projected phase space measurements matched to simulated orbits. *MNRAS*, 463:3083–3095.

Oman, K. A., M. J. Hudson, and P. S. Behroozi
2013. Disentangling satellite galaxy populations using orbit tracking in simulations. *MNRAS*, 431:2307–2316.

Ostriker, J. P. and S. D. Tremaine
1975. Another evolutionary correction to the luminosity of giant galaxies. *ApJL*, 202:L113–L117.

Owen, F. N., W. C. Keel, Q. D. Wang, M. J. Ledlow, and G. E. Morrison
2006. A Deep Radio Survey of Abell 2125. III. The Cluster Core: Merging and Stripping. *AJ*, 131:1974–1988.

Owers, M. S., W. J. Couch, P. E. J. Nulsen, and S. W. Randall
2012. Shocking Tails in the Major Merger Abell 2744. *ApJL*, 750:L23.

Peng, Y.-j., S. J. Lilly, K. Kovač, M. Bolzonella, L. Pozzetti, A. Renzini, G. Zamorani, O. Ilbert, C. Knobel, A. Iovino, C. Maier, O. Cucciati, L. Tasca, C. M. Carollo, J. Silverman, P. Kampczyk, L. de Ravel, D. Sanders, N. Scoville, T. Contini, V. Mainieri, M. Scodeggio, J.-P. Kneib, O. Le Fèvre, S. Bardelli, A. Bongiorno, K. Caputi, G. Coppa, S. de la Torre, P. Franzetti, B. Garilli, F. Lamareille, J.-F. Le Borgne, V. Le Brun, M. Mignoli, E. Perez Montero, R. Pello, E. Ricciardelli, M. Tanaka, L. Tresse, D. Vergani, N. Welikala, E. Zucca, P. Oesch, U. Abbas, L. Barnes, R. Bordoloi, D. Bottini, A. Cappi, P. Cassata, A. Cimatti, M. Fumana, G. Hasinger, A. Koekemoer, A. Leauthaud, D. Maccagni, C. Marinoni, H. McCracken, P. Memeo, B. Meneux, P. Nair, C. Porciani, V. Presotto, and R. Scaramella
2010. Mass and Environment as Drivers of Galaxy Evolution in SDSS and zCOSMOS and the Origin of the Schechter Function. *ApJ*, 721:193–221.

Penzias, A. A. and R. W. Wilson
1965. A Measurement of Excess Antenna Temperature at 4080 Mc/s. *ApJ*, 142:419–421.

Perlmutter, S. and A. Riess
1999. Cosmological parameters from supernovae: Two groups' results agree. In *COSMO-98*, D. O. Caldwell, ed., volume 478 of *American Institute of Physics Conference Series*, Pp. 129–142.

Prada, F., A. A. Klypin, A. J. Cuesta, J. E. Betancort-Rijo, and J. Primack
2012. Halo concentrations in the standard Λ cold dark matter cosmology. *MNRAS*, 423:3018–3030.

Press, W. H. and P. Schechter
1974. Formation of Galaxies and Clusters of Galaxies by Self-Similar Gravitational Condensation. *ApJ*, 187:425–438.

Sandage, A.
1961. *The Hubble Atlas of Galaxies*.

Schaefer, A. L., S. M. Croom, J. T. Allen, S. Brough, A. M. Medling, I.-T. Ho, N. Scott, S. N. Richards, M. B. Pracy, M. L. P. Gunawardhana, P. Norberg, M. Alpaslan, A. E. Bauer, K. Bekki, J. Bland-Hawthorn, J. V. Bloom, J. J. Bryant, W. J. Couch, S. P. Driver, L. M. R. Fogarty, C. Foster, G. Goldstein, A. W. Green, A. M. Hopkins, I. S. Konstantopoulos, J. S. Lawrence, A. R. López-Sánchez, N. P. F. Lorente, M. S. Owers, R. Sharp, S. M. Sweet, E. N. Taylor, J. van de Sande, C. J. Walcher, and O. I. Wong
2017. The SAMI Galaxy Survey: spatially resolving the environmental quenching of star formation in GAMA galaxies. *MNRAS*, 464:121–142.

Simard, L.
1998. GIM2D: an IRAF package for the Quantitative Morphology Analysis of Distant Galaxies. In *Astronomical Data Analysis Software and Systems VII*, R. Albrecht, R. N. Hook, and H. A. Bushouse, eds., volume 145 of *Astronomical Society of the Pacific Conference Series*, P. 108.

Simard, L., J. T. Mendel, D. R. Patton, S. L. Ellison, and A. W. McConnachie
2011. A Catalog of Bulge+disk Decompositions and Updated Photometry for 1.12 Million Galaxies in the Sloan Digital Sky Survey. *ApJS*, 196:11.

Smith, R., J. I. Davies, and A. H. Nelson
2010a. How effective is harassment on infalling late-type dwarfs? *MNRAS*, 405:1723–1735.

Smith, R. J., J. R. Lucey, D. Hammer, A. E. Hornschemeier, D. Carter, M. J. Hudson, R. O. Marzke, M. Mouhcine, S. Eftekharzadeh, P. James, H. Khosroshahi, E. Kourkchi, and A. Karick
2010b. Ultraviolet tails and trails in cluster galaxies: a sample of candidate gaseous stripping events in Coma. *MNRAS*, 408:1417–1432.

Smith, S.
1935. Some Notes on the Structure of Elliptical Nebulae. *ApJ*, 82:192.

Strateva, I., Ž. Ivezić, G. R. Knapp, V. K. Narayanan, M. A. Strauss, J. E. Gunn, R. H. Lupton, D. Schlegel, N. A. Bahcall, J. Brinkmann, R. J. Brunner, T. Budavári, I. Csabai, F. J. Castander, M. Doi, M. Fukugita, Z. Győry, M. Hamabe, G. Hennessy, T. Ichikawa, P. Z. Kunszt, D. Q. Lamb, T. A. McKay, S. Okamura, J. Racusin, M. Sekiguchi, D. P. Schneider, K. Shimasaku, and D. York
2001. Color Separation of Galaxy Types in the Sloan Digital Sky Survey Imaging Data. *AJ*, 122:1861–1874.

Tacchella, S., P. Lang, C. M. Carollo, N. M. Förster Schreiber, A. Renzini, A. E. Shapley, S. Wuyts, G. Cresci, R. Genzel, S. J. Lilly, C. Mancini, S. F. Newman, L. J. Tacconi, G. Zamorani, R. I. Davies, J. Kurk, and L. Pozzetti
2015. SINS/zC-SINF Survey of z˜2 Galaxy Kinematics: Rest-frame Morphology, Structure, and Colors from Near-infrared Hubble Space Telescope Imaging. *ApJ*, 802:101.

Tinker, J. L. and A. R. Wetzel
2010. What does Clustering Tell us About the Buildup of the Red Sequence? *ApJ*, 719:88–103.

Toomre, A. and J. Toomre
1972. Galactic Bridges and Tails. *ApJ*, 178:623–666.

van den Bosch, F. C., D. Aquino, X. Yang, H. J. Mo, A. Pasquali, D. H. McIntosh, S. M. Weinmann, and X. Kang
2008. The importance of satellite quenching for the build-up of the red sequence of present-day galaxies. *MNRAS*, 387:79–91.

van der Wel, A., M. Franx, P. G. van Dokkum, R. E. Skelton, I. G. Momcheva, K. E. Whitaker, G. B. Brammer, E. F. Bell, H.-W. Rix, S. Wuyts, H. C. Ferguson, B. P. Holden, G. Barro, A. M. Koekemoer, Y.-Y. Chang, E. J. McGrath, B. Häussler, A. Dekel, P. Behroozi, M. Fumagalli, J. Leja, B. F. Lundgren, M. V. Maseda, E. J. Nelson, D. A. Wake, S. G. Patel, I. Labbé, S. M. Faber, N. A. Grogin, and D. D. Kocevski
2014. 3D-HST+CANDELS: The Evolution of the Galaxy Size-Mass Distribution since z = 3. *ApJ*, 788:28.

von der Linden, A., P. N. Best, G. Kauffmann, and S. D. M. White
2007. How special are brightest group and cluster galaxies? *MNRAS*, 379:867–893.

Wetzel, A. R., J. L. Tinker, and C. Conroy
2012. Galaxy evolution in groups and clusters: star formation rates, red sequence fractions and the persistent bimodality. *MNRAS*, 424:232–243.

Wetzel, A. R., J. L. Tinker, C. Conroy, and F. C. van den Bosch
2013. Galaxy evolution in groups and clusters: satellite star formation histories and quenching time-scales in a hierarchical Universe. *MNRAS*, 432:336–358.

Yoshida, M., M. Yagi, Y. Komiyama, H. Furusawa, N. Kashikawa, Y. Koyama, H. Yamanoi, T. Hattori, and S. Okamura
2008. Strange Filamentary Structures ("Fireballs") around a Merger Galaxy in the Coma Cluster of Galaxies. *ApJ*, 688:918–930.

Zwicky, I. F.
1942. On the Clustering of Nebulae. *ApJ*, 95:555.

Appendices

Appendix A

Simard Model Fits: Consistency Check

In order to check and verify the consistency between the B/T luminosity model fits given by Simard et al. (2011), we plot the B/T from both, $n_b = 4$ and free-n_b models. Fig. A.1 shows an excess of objects that are disc dominant in the $n4$ model yet are given a considerable bulge component in the free-n_b model. We did a visual inspection for about a dozen objects falling between $0.5 \leq (B/T)_{free-n_b} \leq 1.0$ and $0.0 \leq (B/T)_{n4} \leq 0.2$ and found most objects to be disc dominant systems with a very small bulge component. This bulge component was certainly not sufficiently luminous to yield a B/T greater than 0.5 (in the free-n_b model). The visual investigation is strengthened by plotting the Sérsic indices distribution from the pure Sérsic fit model for objects with B/T > 0.5 from free-n_b model and B/T < 0.2 from n_b fit. Fig. A.2 shows the all such objects have a Sérsic index between $0.5 \leq n \leq 2$. This showed that they are indeed disc dominant systems. Hence, in order to understand the free-n_b model fits, we plotted the surface brightness profiles of such objects.

We found two main kinds of surface brightness profiles. Type 2 (based on the Morphological classification used by Driver et al. (2006)) profile shown in Fig. A.3 is a case where the galaxy only has a single component. The bulge fit in reality is a disc as it doesn't fall off as sharply as expected for a bulge (high Sérsic index) but rather falls of more slowly and the disc fit doesn't matter as it is much more dimmer. In this case, the bulge fit from the free-n_b model is a disc in reality and the disc profile technically should be non-existent. The correction for such profiles is to consider their bulge luminosity as disc-luminosity and vice versa.

Type 4 profile is a case where the galaxy is an actual two component system consisting of a bulge and a disc as shown in Fig. A.4. For the central region (before the intersection) the disc profile is more brighter than the bulge and falls off much faster after intersection while in reality, the bulge fit should be brighter in the central

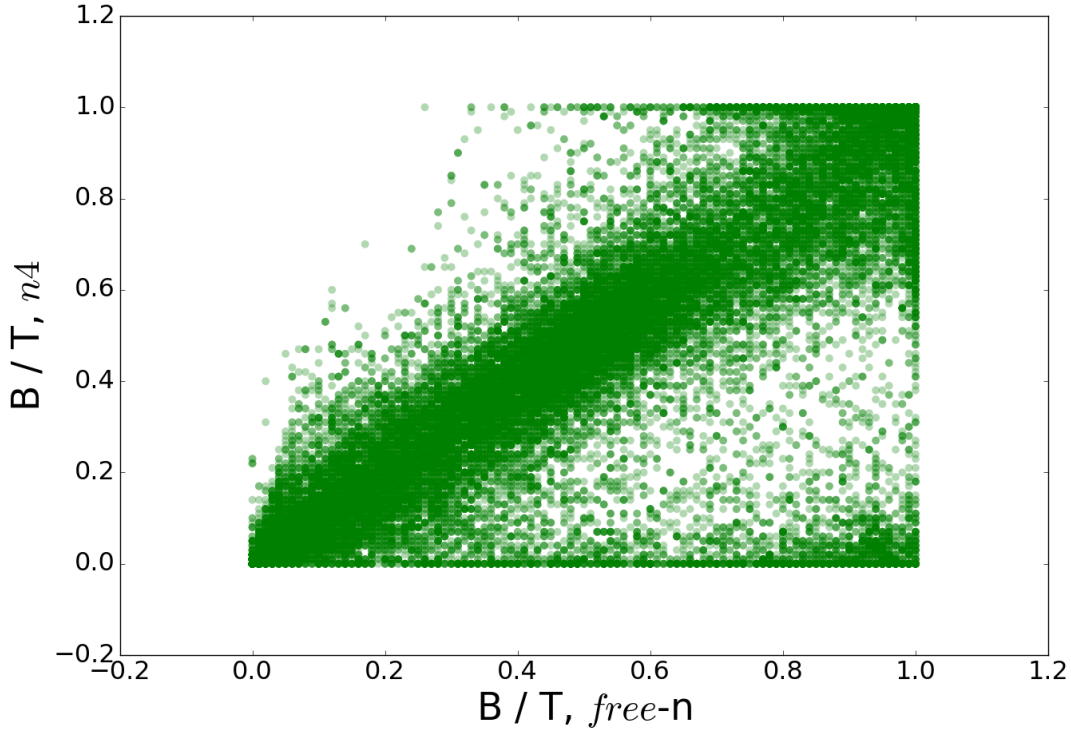

Figure A.1: B/T comparison between Simard's $n4$ and free-n_b *models.*

region and should drop off faster than the disk after intersection. Hence in the case of this type we conclude that the two profiles: bulge and disc have been switched.

A quick fix for B/T from free-n_b model for the cases of both Type 1 and 2 profiles is to reassign them with a new B/T given by: $(B/T)_{new}$ = 1-$(B/T)_{old}$ where $(B/T)_{old}$ is the original value.

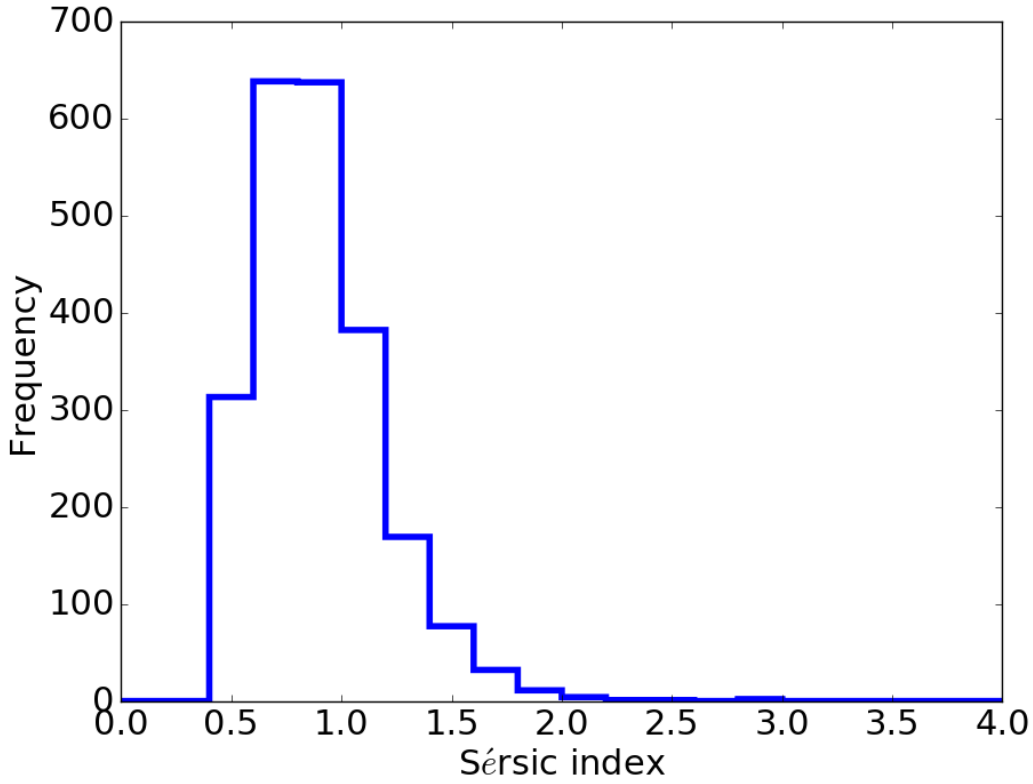

Figure A.2: Sérsic index, n, for $B/T_{free-n_b} > 0.5$ and $B/T_{n4} < 0.2$ from Simard pure Sérsic fit.

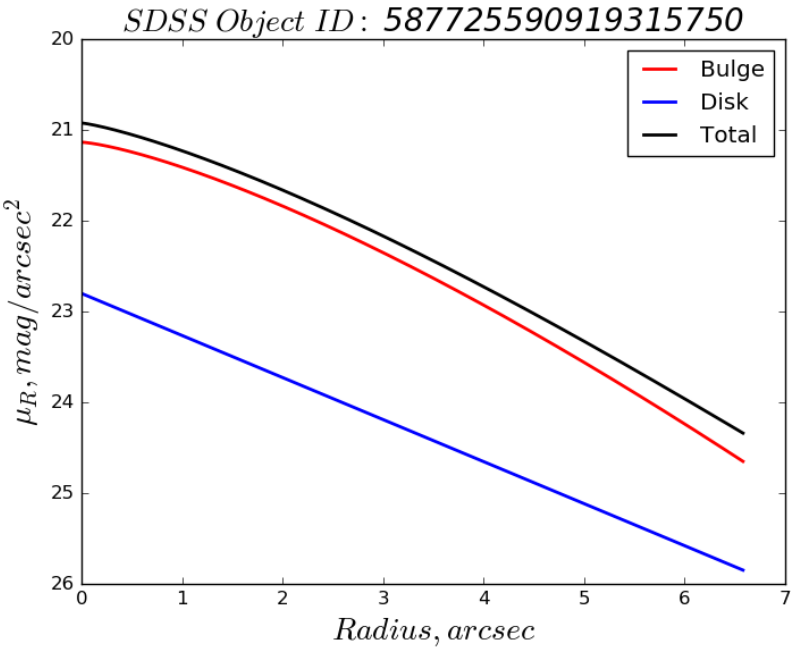

Figure A.3: Surface brightness profile of Type 2.

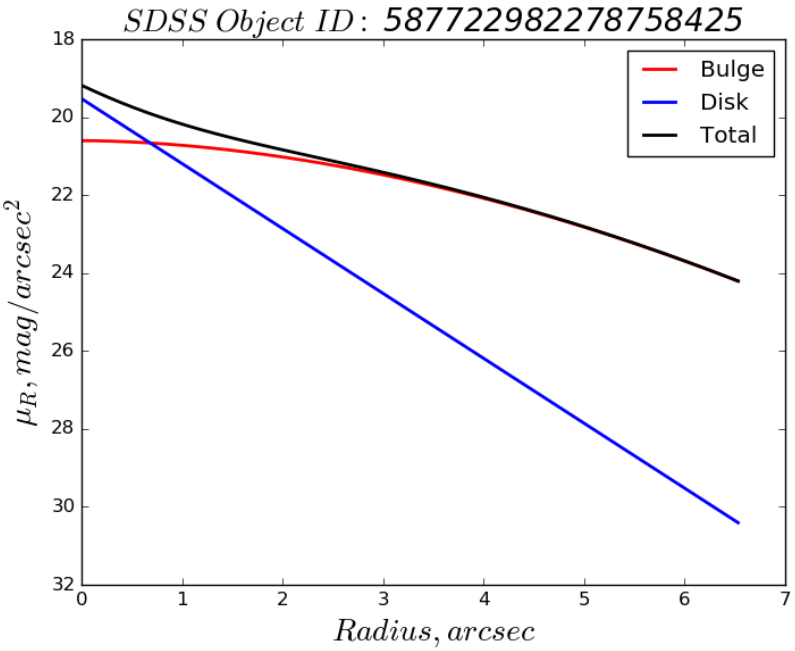

Figure A.4: Surface brightness profile of Type 4.

Appendix B

Data Cleaning: B/T reassignment

The disc colour distributions for B/T >0.9 and B/T<0.9 objects are shown in red and green histograms respectively. We find the disc colors unreliable for 1076/48454 objects. In the red histogram, the objects with negative colours are representative of the SDSS magnitude where *r-band* absolute magnitude, M_r is greater than *g-band* absolute magnitude M_g. Upon visual inspection, it was found that these objects are purely a bulge component with a negligible disc size thus the disc component fits for such objects are unreliable. To fix this, we change the B/T > 0.9 to B/T $= 1$ and B/T < 0.1 to B/T $= 0$. Similarly, we also notice negative colors for bulges with B/T <0.1 (not shown), which is a manifestation of a fit to a very small bulge component. All such satellites with B/T < 0.1 are reassigned a B/T $= 0$ in this case to avoid spurious colors.

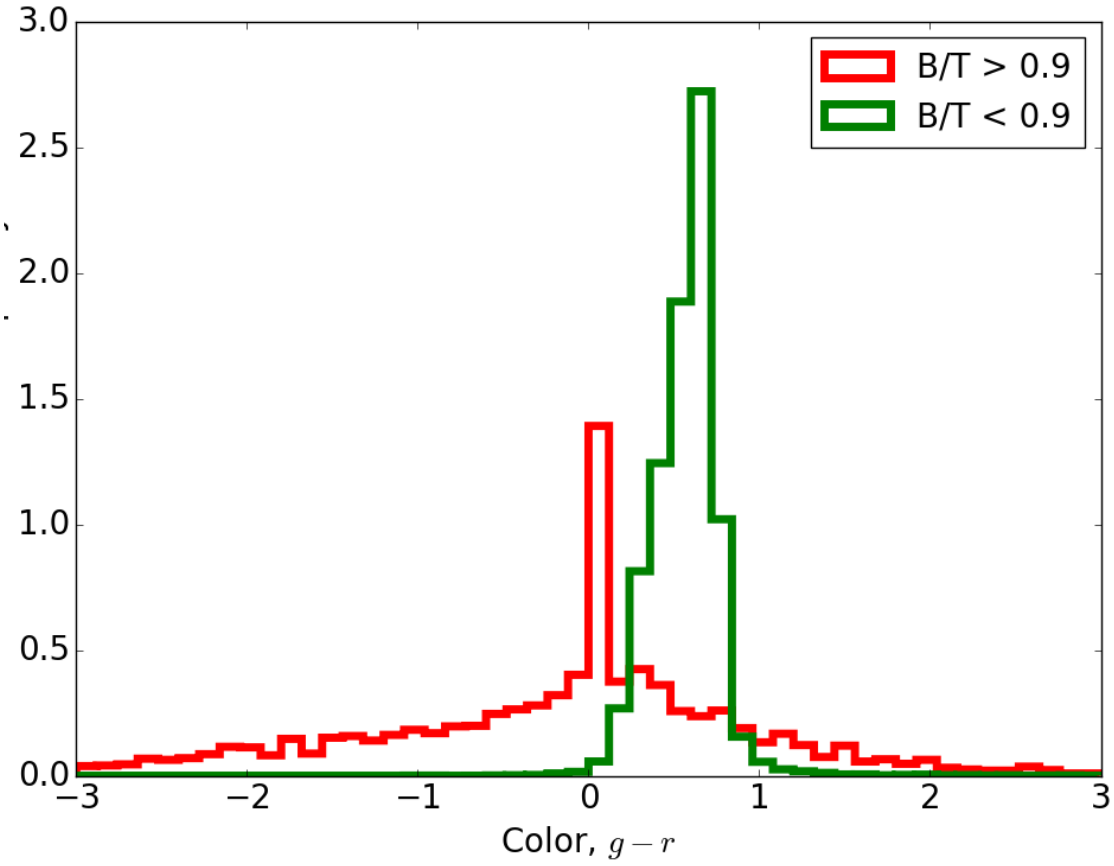

Figure B.1: Disc color distribution for object with B/T >0.9 and B/T<0.9 from Simard $n4$ model fit.

Appendix C

Interloper Population: Metallicity Calculation

In order to get a realistic account of the stellar metallicity of galaxies in our sample, we use results from Gonzalez et al. (2014) (hereafter G14). They use a sample of 300 CALIFA galaxies of all morphologies. They find that metallicity is dependent on both local and global effects. Local effects are represented by stellar surface mass density $\mu_\star$ whereas global effects are controlled by the total mass of the galaxy, $M_\star$. Their findings suggest metallicity to monotonically increase with local stellar mass density modulated by the total stellar mass. In addition to this, they also discriminate between the bulge and disc components defined by radial profile of galaxies cut at R $<$ and R $>$ 0.5 half-light radius respectively. We use their results from Fig. 3(b) which demonstrates the disc component and manually find the slope and intercept of the curves. We calculate the average metallicity of the disc component for the interloper population of our sample using the following expression.

$$\langle Z \rangle = \frac{\int Z(r)\mu_\star(r) r dr}{\int \mu_\star(r) r dr} \tag{C.1}$$

where Z(r) is calculated from Fig. 3(b) by finding the slope, b, and intercept, c, of G14 using:

$$Z(r) = 10^b \mu_\star^c \tag{C.2}$$

Here $\mu_\star(r)$ is given by:

$$\mu_\star(r) = \mu_0 e^{(-r/r_d)} \tag{C.3}$$

with μ_0 as:

$$\mu_0 = \frac{M_{Tot,Disk}}{\int_0^{r_d} re^{(-r/r_d)dr}} \tag{C.4}$$

where $M_{Tot,Disk}$ and r_d are the total stellar mass of the disc and the disc scale length respectively.

Once the average stellar metallicity for a given galaxy is calculated, we find the median metallicity for all the galaxies in our sample which comes out to be 0.0125. This value is then used in the *EzGal* code for the rest of the analysis.